

THE *SPITZER* c2d SURVEY OF LARGE, NEARBY, INTERSTELLAR CLOUDS. XII. THE PERSEUS YSO POPULATION AS OBSERVED WITH IRAC AND MIPS

KAISA E. YOUNG¹, CHADWICK H. YOUNG¹, SHIH-PING LAI², MICHAEL M. DUNHAM³, AND NEAL J. EVANS II⁴¹ Department of Physical Sciences, Nicholls State University, P.O. Box 2022, Thibodaux, LA 70310, USA; kaisa.young@nicholls.edu, chad.young@nicholls.edu² Institute of Astronomy and Department of Physics, National Tsing Hua University, Hsinchu 30013, Taiwan; slai@phys.nthu.edu.tw³ Harvard-Smithsonian Center for Astrophysics, 60 Garden Street, MS 78, Cambridge, MA 02138, USA; mdunham@cfa.harvard.edu⁴ Department of Astronomy, University of Texas at Austin, 2515 Speedway, Stop C1400, Austin, TX 78712, USA; nje@astro.as.utexas.edu

Received 2014 December 15; accepted 2015 May 7; published 2015 July 14

ABSTRACT

The *Spitzer Space Telescope* mapped the Perseus molecular cloud complex with the Infrared Array Camera (IRAC) and the Multi-Band Imaging Photometer for *Spitzer* (MIPS) as part of the c2d *Spitzer* Legacy project. This paper combines the observations from both instruments giving an overview of low-mass star formation across Perseus from 3.6 to 70 μm . We provide an updated list of young stellar objects (YSOs) with new classifications and source fluxes from previous works, identifying 369 YSOs in Perseus with the *Spitzer* data set. By synthesizing the IRAC and MIPS maps of Perseus and building on the work of previous papers in this series, we present a current census of star formation across the cloud and within smaller regions. Sixty-seven percent of the YSOs are associated with the young clusters NGC 1333 and IC 348. The majority of the star formation activity in Perseus occurs in the regions around the clusters to the eastern and western ends of the cloud complex. The middle of the cloud is nearly empty of YSOs despite containing regions of high visual extinction. The western half of Perseus contains three-quarters of the total number of embedded YSOs (Class 0+I and Flat spectral energy distribution sources) in the cloud and nearly as many embedded YSOs as Class II and III sources. Class II and III objects greatly outnumber Class 0+I objects in eastern Perseus and IC 348. These results are consistent with previous age estimates for the clusters. Across the cloud, 56% of YSOs and 91% of the Class 0+I and Flat sources are in areas where $A_V \geq 5$ mag, indicating a possible extinction threshold for star formation.

Key words: dust, extinction – infrared: stars – ISM: individual objects (IC 348, NGC 1333 Perseus) – stars: formation

Supporting material: machine-readable and VO tables

1. INTRODUCTION

Large-scale studies of nearby molecular clouds provide the ability to study the environment of the earliest stages of star formation. The “From Molecular Cores to Planet Forming Disks” (c2d) *Spitzer* Legacy project (Evans et al. 2003) used the *Spitzer Space Telescope* (Werner et al. 2004) to map five large molecular clouds with the Infrared Array Camera (IRAC; Fazio et al. 2004) and the Multi-Band Imaging Photometer for *Spitzer* (MIPS; Rieke et al. 2004) including Serpens, Chamaeleon II, Lupus, Ophiuchus, and Perseus. The c2d team’s data and results for all five large clouds were compared and summarized in Evans et al. (2009), hereafter E09.

We present a study of the complete IRAC and MIPS c2d maps of the Perseus molecular cloud. Our work synthesizes the data sets first presented by Jørgensen et al. (2006) and Rebull et al. (2007) putting the full *Spitzer* observations in the context of more recent work on Perseus. This paper gives an overview of low-mass star formation across the varied environments in Perseus from 3.6 to 70 μm . We provide an updated list of young stellar objects (YSOs) with newly corrected photometry, spectral indices, and classifications.

Perseus is a well-known and a much-studied cloud (e.g., Sargent 1979; Ladd et al. 1993; Kirk et al. 2006; Enoch et al. 2007) because it presents a range of star formation environments. Perseus contains two young clusters, IC 348 and NGC 1333, as well as several small dense clumps of the type that often produce one or a few stars (B1, B5, L1448, and L1455). Perseus is near the middle of the spectrum of star formation in large clouds that span from a low density (e.g.,

Chamaeleon II) to a high density (e.g., Serpens) of YSOs (Evans et al. 2009). Perseus is not currently forming very high-mass (mid-B or earlier spectral type) stars, although, IC 348 is known to contain a B5 V star (BD+31°634). Therefore, Perseus has been called a “typical” cloud in the study of the early phases of low-mass star formation (Enoch et al. 2006).

Perseus also contains protostellar cores, very low luminosity objects (VeLLOs), and potentially very young YSOs that are too deeply embedded to have been detected by *Spitzer*. Six candidate first hydrostatic cores have been identified in Perseus (e.g., Chen et al. 2010; Enoch et al. 2010; Pineda et al. 2011). Dunham et al. (2008) identify numerous low-luminosity embedded protostars as well as VeLLOs in the cloud. Enoch et al. (2006) combined the *Spitzer* map with a 1.1 mm Bolocam dust continuum map of Perseus from the Caltech Submillimeter Observatory. They discuss the properties of prestellar (Enoch et al. 2008) and Class 0 and I cores (Enoch et al. 2009) identified with the *Spitzer* and Bolocam data. Perseus was also mapped in the submillimeter using SCUBA at the James Clerk Maxwell Telescope (Hatchell et al. 2005; Kirk et al. 2006). Discussion of the *Spitzer* sources in relation to the SCUBA cores can be found in Hatchell et al. (2007) and Jørgensen et al. (2007). More recently, Sadavoy et al. (2014) identified 28 candidate Class 0 sources in Perseus using the *Herschel Space Observatory*. Four of these sources had not been previously identified with *Spitzer*.

The IRAC and MIPS data sets for Perseus were analyzed individually by Jørgensen et al. (2006) and Rebull et al. (2007) respectively. This is the twelfth paper in a series presenting

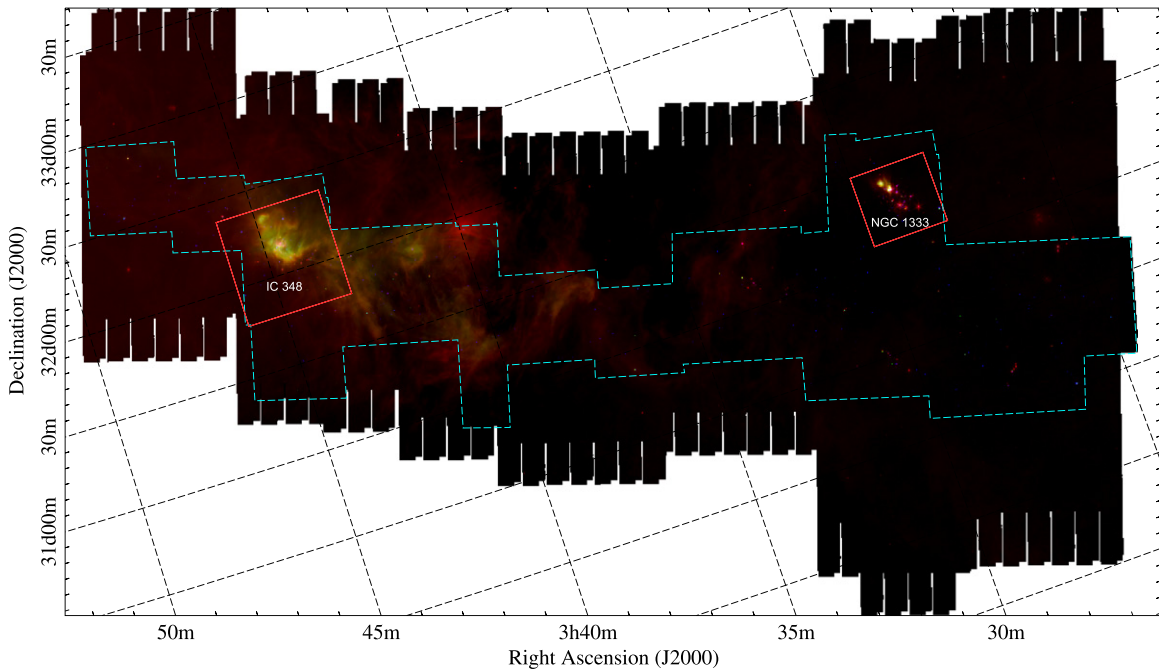


Figure 1. Three-color (blue = $4.5\ \mu\text{m}$, green = $8\ \mu\text{m}$, and red = $24\ \mu\text{m}$) mosaic of Perseus. Edges of the image are the MIPS scan region. The IRAC observation area is given by the cyan dashed line. The red boxes indicate the IC 348 and NGC 1333 cluster regions as described in Section 3.

original *Spitzer* data of the five large molecular clouds mapped by the c2d team. We adopt the same distance of 250 ± 50 pc for Perseus (Enoch et al. 2006) for consistency with previous work by the c2d team. However, very long baseline interferometry studies of H_2O masers in nearby star-forming regions give a slightly closer distance to the western end of Perseus: 235 ± 18 pc for NGC 1333 (Hirota et al. 2008) and 232 ± 18 pc to L1448 (Hirota et al. 2011).

We follow the same data reduction and analysis procedures laid out in previous papers in the series and briefly described in the following sections. We have updated the c2d list of YSOs in Perseus, providing new extinction-corrected photometry, and discuss the classification and distribution of YSOs both within and outside the clusters in the context of the extended emission and visual extinction in Perseus.

2. OBSERVATIONS AND DATA

The Perseus molecular cloud was mapped with two of the *Spitzer Space Telescope's* instruments, IRAC and MIPS. Figure 1 is a three-color composite map of Perseus from the IRAC 4.5 and $8\ \mu\text{m}$ and MIPS $24\ \mu\text{m}$ data. The *Spitzer* maps cover 3.86 square degrees in the IRAC observation wavelengths of 3.6, 4.5, 5.8, and $8.0\ \mu\text{m}$ and approximately 10.5 square degrees with MIPS at 24, 70, and $160\ \mu\text{m}$. However, due to the nature of the detector, the $160\ \mu\text{m}$ maps are not complete and provide only limited photometry for a portion of the YSOs. Therefore, our discussion will be limited to data from 3.6 to $70\ \mu\text{m}$. Rebull et al. (2007) discussed the $160\ \mu\text{m}$ mosaic. In Figure 1, the edges of the image are the MIPS scan boundaries and the IRAC observation area is denoted by the dashed lines. We will focus on the area where the two maps overlap, namely the nearly 4 square degrees observed by IRAC.

The outline of the Perseus mapped region was selected using the $A_V = 2$ mag contour from ^{13}CO extinction maps of Padoan et al. (1999). The c2d team chose this criteria in order to

observe the regions of densest gas and dust in the cloud complex and, by association, observe all of the young and forming stars in Perseus. A correlation also exists between ^{13}CO and near-infrared dust extinction (Kainulainen et al. 2011). Pineda et al. (2008) showed that the ^{13}CO column density is correlated with visual extinction (A_V) in Perseus for $A_V < 10$ mag. However, Heiderman et al. (2010) concluded that, while ^{13}CO may be a good tracer of gas surface density, it is not linearly correlated with visual extinction in Perseus when considering A_V up to 25 mag and, using standard conversion factors, may underestimate mass.

The IRAC maps fit tightly to the $A_V = 2$ mag outline, whereas MIPS was able to scan over a much larger area in less observing time due to the design of the instrument. NGC 1333 and IC 348 were mapped separately from the c2d map in conjunction with the *Spitzer* Guaranteed Time Observers program (GTOs; Lada et al. 2006; Gutermuth et al. 2008). The GTO maps have been combined with the larger c2d maps and are included in this analysis.

The IRAC and MIPS observations of Perseus were discussed in detail in Jørgensen et al. (2006) and Rebull et al. (2007) respectively. We only discuss pertinent details of the observations here. Each instrument mapped Perseus twice in separate time epochs anywhere from several hours to 7 months apart, depending on the region, to identify and eliminate asteroids and artifacts. The raw data were processed through the c2d data reduction pipeline to create mosaic maps, reduce instrumental effects, and produce a band-merged source catalog for Perseus that includes both 2MASS and *Spitzer* photometry. The fluxes given in the c2d catalog at each IRAC and MIPS band are the average of the single-epoch fluxes (Evans et al. 2007, 2009). The c2d catalogs for Perseus as well as the other molecular clouds and cores included in the survey are available online through the NASA/IPAC Infrared Science Archive (IRSA:c2d 2007). A complete description of the data processing and source extraction for all of the c2d data can be found in the first

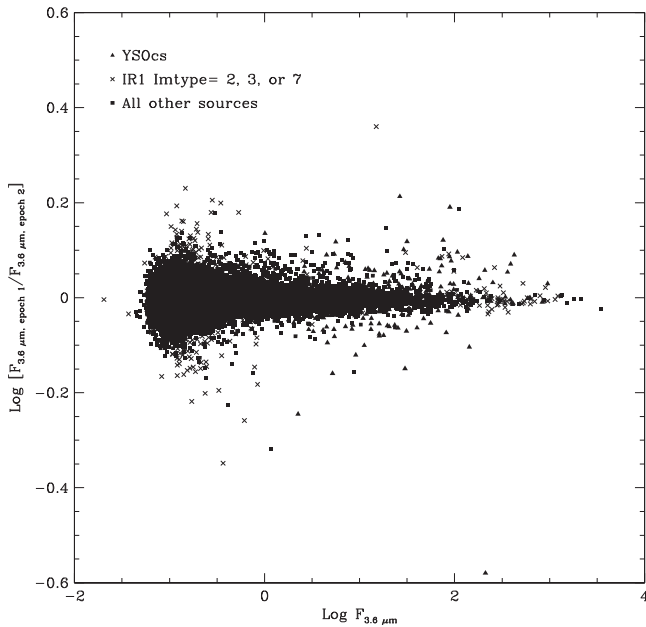


Figure 2. Log of the ratio of fluxes in the IRAC 1 band ($3.6 \mu\text{m}$) between the two observation epochs vs. the log of the $3.6 \mu\text{m}$ flux in mJy from the combined epochs for all sources where the uncertainty is less than 10% of the flux in single epoch. Sources identified as YSO candidates by the c2d team are triangles. Crosses represent sources flagged as extended, double, or with a signal-to-noise ratio that was too small to determine their shape (Imtype = 2, 3 or 7) in the IRAC 1 map as discussed in Section 2. All other source types, including stars, are squares.

papers in this series (e.g., Young et al. 2005; Harvey et al. 2006) and in the final c2d data delivery document (Evans et al. 2007).

Figure 2 plots the ratio of observed fluxes at $3.6 \mu\text{m}$ (IRAC Band 1) between the two observation epochs versus the $3.6 \mu\text{m}$ flux derived from the combined epochs for all sources in the cloud with a single epoch flux-to-uncertainty ratio greater than 10. The flux measurements are very consistent, differing by less than 15% between the epochs with an average flux ratio of $\log [F_{(3.6 \mu\text{m}, \text{epoch1})} / F_{(3.6 \mu\text{m}, \text{epoch2})}] = -0.0032$. Figure 2 shows a slightly larger spread in the flux ratios ($-0.2 < \log [F_{(3.6 \mu\text{m}, \text{epoch1})} / F_{(3.6 \mu\text{m}, \text{epoch2})}] < 0.2$) for the faintest sources ($F_{3.6 \mu\text{m}} < 1 \text{ mJy}$). The few sources with more extreme flux ratios between epochs were mostly flagged in the data processing as extended, double, or with a signal-to-noise ratio that was too small to determine their shape (Imtype = 2, 3, or 7; Evans et al. 2007). These Imtypes are indicated as X's in Figure 2, where one can see that the outliers fall mostly in these categories.

Three objects classified by c2d as YSOs (see Section 3) have a large ratio of $3.6 \mu\text{m}$ fluxes between the first and second observations (triangle outliers in Figure 2). The variation in flux between the two observation epochs for these objects is likely not physical. One YSO in the IC 348 region was flagged with an uncertainty ratio too low to accurately determine shape (index number 348 in Table 1). Another YSO in IC 348 (424 in Table 1) has a relatively low flux at $3.6 \mu\text{m}$, $\log F_{3.6 \mu\text{m}} = 0.068$, placing it at the edge of the spread in Figure 2. This object is also situated in extended nebulosity near a source with a large $3.6 \mu\text{m}$ flux. The third YSO outlier (209 in Table 2) has a combined epoch flux of 39 mJy at $3.6 \mu\text{m}$ and a $\log [F_{(3.6 \mu\text{m}, \text{epoch1})} / F_{(3.6 \mu\text{m}, \text{epoch2})}] = 0.213$ for observations 7

months apart. YSO 209 is a Class 0+I object (see Section 4) located in the NGC 1333 region, but again is potentially confused with bright nebulosity.

3. YSO SELECTION

A major goal of the c2d program was to identify YSOs in large molecular clouds. We follow the method of previous papers in this series for selecting YSO candidates in Perseus, in which YSOs are distinguished from reddened background galaxies using color-color and color-magnitude diagrams in the 2MASS (H and K), IRAC (4.5 and $8 \mu\text{m}$), and MIPS ($24 \mu\text{m}$) bands. This method is described here briefly, however, a detailed description can be found in the c2d data delivery document (Evans et al. 2007) and by Harvey et al. (2007).

The c2d data were compared with a galaxy sample in the ELAIS N1 field from the *Spitzer* Wide-area Infrared Extragalactic (SWIRE) catalog (Lonsdale et al. 2003). ELAIS N1 is well above the Galactic plane and not expected to contain any YSOs or molecular clouds. The SWIRE data was used to eliminate confusion of reddened background galaxies with YSOs, however, it does not control for reddened background stars in our own Galaxy. IRAC and MIPS maps of the field observed by the SWIRE team were resampled to match the c2d sensitivity and reprocessed in the c2d pipeline so accurate color comparisons could be made. In addition, the SWIRE data were also reddened using the extinction profile of Perseus generated from *Spitzer* data (Figure 3). Therefore, galaxies in the SWIRE field would appear reddened as if behind a Perseus-like molecular cloud. The reprocessed SWIRE data were plotted in infrared color-color and color-magnitude spaces to determine the positions of galaxies in the diagrams. This process resulted in cutoff limits in each color-color and color-magnitude space to divide YSOs from galaxies.

The color-color and color-magnitude diagrams used for YSO selection in Perseus are in Figure 4. The lines in each color-color or color-magnitude space are the cutoffs that define the YSO candidate criterion in the various color-magnitude spaces created by comparison with the SWIRE data and are the same as those presented and discussed by Harvey et al. (2007). The c2d team constructed the cutoffs in the color-magnitude diagrams to be smooth, exponentially decaying probabilities around the lines in Figure 4 so that sources far below the cutoffs are assigned the highest probability of being extragalactic. The probability of extragalactic contamination is highest in the center of the ellipses in the [24] versus [8.0]–[24] diagrams and decreases radially.

Perseus sources with infrared colors that were consistent with dust emission rather than extinct background stars were assigned an unnormalized total “probability” that the source is extragalactic. This proxy for probability is formed from the product of the individual probabilities from the color-magnitude diagrams in Figure 4 and factors based on source properties such as $K - [4.5]$ color, MIPS flux density, and whether it was found to be extended at 3.6 and $4.5 \mu\text{m}$ (Harvey et al. 2007). The cutoffs for $K - [4.5]$ color are also shown in Figure 4. Bluer colors reflect a higher probability that the source is extragalactic.

In Figures 3–5 and the following text, we divide Perseus into three distinct regions for comparison of the YSO properties. The sources associated with the IC 348 and NGC 1333 clusters are shown separately from the “Remaining Cloud” (hereafter RC), which includes all the other sources, such as B1 and

Table 1
YSOs in the IC 348 Region

E09 Index	Source Name (SSTc2d +)	α	Class	IRAC ^a 3.6 μm	IRAC 4.5 μm	IRAC 5.8 μm	IRAC 8.0 μm	MIPS ^a 24 μm	MIPS 70 μm
337	J034313.70+320045.2	-1.15	II	16 \pm 1.1	19 \pm 1.2	16 \pm 1.0	21 \pm 1.3	26 \pm 2.7	...
340	J034323.57+321225.9	-1.52	II	4.9 \pm 0.36	4.0 \pm 0.31	3.2 \pm 0.28	3.0 \pm 0.28	2.8 \pm 0.37	...
341	J034325.48+315516.5	-1.33	II	15 \pm 1.1	11 \pm 0.86	7.8 \pm 0.70	5.9 \pm 0.69	17 \pm 1.9	...
342	J034328.21+320159.1	-1.39	II	63 \pm 4.3	65 \pm 4.4	46 \pm 3.6	46 \pm 3.7	45 \pm 4.7	...
343	J034328.46+320505.8	-1.19	II	8.2 \pm 0.60	7.6 \pm 0.54	6.3 \pm 0.48	7.6 \pm 0.54	11 \pm 1.2	...
344	J034329.43+315219.5	0.41	0+I	7.7 \pm 0.53	13 \pm 0.71	20 \pm 1.0	43 \pm 2.1	180 \pm 20	260 \pm 33
345	J034336.02+315009.0	-0.18	Flat	3.7 \pm 0.26	4.4 \pm 0.28	5.2 \pm 0.31	9.5 \pm 0.47	30 \pm 3.1	...
347	J034344.63+320817.8	-0.93	II	22 \pm 1.6	17 \pm 1.4	12 \pm 1.2	12 \pm 1.2	110 \pm 12	170 \pm 44
348	J034345.17+320358.6	0.11	Flat	300 \pm 22	190 \pm 19	250 \pm 18	140 \pm 17	850 \pm 90	940 \pm 100
349	J034348.83+321551.5	-1.07	II	10 \pm 0.79	9.9 \pm 0.71	10 \pm 0.69	13 \pm 0.8	15 \pm 1.6	...
350	J034350.96+320324.7	1.39	0+I	0.49 \pm 0.04	1.5 \pm 0.12	1.9 \pm 0.18	3.4 \pm 0.2	62 \pm 6.6	...
351	J034351.02+320308.1	-0.29	Flat	9.8 \pm 0.85	5.4 \pm 0.85	17 \pm 1.2	2.9 \pm 0.24	52 \pm 5.5	2000 \pm 290
353	J034355.24+315532.1	-0.99	II	52 \pm 3.7	43 \pm 3.1	31 \pm 2.6	25 \pm 2.5	100 \pm 10	...
354	J034355.28+320753.3	-1.09	II	5.0 \pm 0.38	4.8 \pm 0.34	4.6 \pm 0.34	5.6 \pm 0.37	5.9 \pm 0.66	...
355	J034356.03+320213.3	-1.20	II	210 \pm 14	200 \pm 14	170 \pm 11	190 \pm 13	210 \pm 22	...
357	J034356.84+320304.7	1.83	0+I	0.07 \pm 0	0.27 \pm 0.08	0.66 \pm 0.08	0.79 \pm 0.16	13 \pm 1.4	3400 \pm 460
358	J034357.23+320133.7	-1.28	II	7.8 \pm 0.53	7.4 \pm 0.51	5.9 \pm 0.43	6.2 \pm 0.46	6.5 \pm 0.75	...
362	J034358.57+321727.5	-1.10	II	33 \pm 2.6	31 \pm 2.2	25 \pm 1.9	31 \pm 2.2	52 \pm 5.4	...
363	J034358.92+321127.2	-0.84	II	46 \pm 3.5	45 \pm 3.2	38 \pm 2.8	50 \pm 3.3	170 \pm 17	...
364	J034359.10+321421.2	-1.28	II	20 \pm 1.5	21 \pm 1.4	16 \pm 1.2	19 \pm 1.3	27 \pm 3.0	...
366	J034359.65+320154.1	-0.90	II	1200 \pm 84	1300 \pm 97	1300 \pm 74	1800 \pm 110	1500 \pm 160	1700 \pm 190
367	J034359.88+320441.4	-1.10	II	3.9 \pm 0.28	3.2 \pm 0.25	2.8 \pm 0.23	3.2 \pm 0.26	7 \pm 0.79	...
368	J034400.48+320432.7	-0.82	II	4.3 \pm 0.29	4.0 \pm 0.27	3.7 \pm 0.25	4.4 \pm 0.29	9.2 \pm 1.1	...
369	J034401.57+322358.9	-1.21	II	6.3 \pm 0.47	5.6 \pm 0.41	4.5 \pm 0.39	5.4 \pm 0.40	8.1 \pm 0.88	...
370	J034402.40+320204.9	1.47	0+I	1.1 \pm 0.07	2.6 \pm 0.2	4.8 \pm 0.34	8.4 \pm 0.59	130 \pm 14	870 \pm 120
371	J034402.63+320159.5	0.92	0+I	1.2 \pm 0.08	3.8 \pm 0.22	5.1 \pm 0.25	8.0 \pm 0.39	63 \pm 7.5	...
372	J034402.92+315227.7	-1.31	II	5.5 \pm 0.39	4.7 \pm 0.35	4.3 \pm 0.32	4.7 \pm 0.35	4.4 \pm 0.51	...
373	J034405.78+320001.1	-0.92	II	5.7 \pm 0.40	5.2 \pm 0.34	4.7 \pm 0.32	5.7 \pm 0.36	9.9 \pm 1.1	...
374	J034405.78+320028.5	-0.64	II	55 \pm 3.8	65 \pm 4.0	68 \pm 3.8	68 \pm 3.7	31 \pm 3.3	...
375	J034406.01+321532.1	-1.16	II	3.0 \pm 0.21	2.7 \pm 0.21	2.7 \pm 0.20	2.8 \pm 0.22	2.9 \pm 0.38	...
377	J034406.80+320754.0	-1.15	II	13 \pm 0.95	11 \pm 0.82	9.5 \pm 0.77	11 \pm 0.8	15 \pm 1.6	...
378	J034409.16+320709.3	-2.36	III	98 \pm 7.2	66 \pm 5.9	46 \pm 5.4	37 \pm 5.3	10 \pm 1.1	...
379	J034409.20+320237.8	0.61	0+I	17 \pm 1.2	34 \pm 1.8	36 \pm 1.9	63 \pm 3.2	320 \pm 35	280 \pm 59
380	J034410.13+320404.5	-1.11	II	10 \pm 0.72	9.3 \pm 0.69	8.3 \pm 0.64	9.0 \pm 0.73	16 \pm 1.9	...
381	J034411.63+320313.1	-1.39	II	92 \pm 6.5	68 \pm 5.6	68 \pm 5.0	70 \pm 5.3	50 \pm 5.4	...
382	J034412.98+320135.5	0.29	Flat	220 \pm 14	590 \pm 40	620 \pm 32	790 \pm 47	1800 \pm 200	4700 \pm 510
383	J034415.84+315936.7	-1.03	II	4.0 \pm 0.27	3.4 \pm 0.26	3.1 \pm 0.24	4.1 \pm 0.28	7.6 \pm 0.84	...
384	J034418.10+321053.5	-1.03	II	50 \pm 3.6	41 \pm 2.9	32 \pm 2.3	35 \pm 2.5	39 \pm 4.2	...
385	J034418.17+320457.0	-0.92	II	130 \pm 8.9	83 \pm 7.4	93 \pm 6.9	79 \pm 6.8	580 \pm 61	...
386	J034418.21+320959.3	-1.45	II	8.2 \pm 0.63	6.9 \pm 0.53	5.6 \pm 0.48	5.2 \pm 0.48	9.0 \pm 1.0	...
387	J034418.27+320732.5	-1.49	II	3.8 \pm 0.27	2.8 \pm 0.24	2.1 \pm 0.23	2.2 \pm 0.24	1.9 \pm 0.42	...
388	J034418.59+321253.1	-1.01	II	37 \pm 2.8	37 \pm 2.5	35 \pm 2.4	36 \pm 2.5	36 \pm 3.9	...
389	J034419.14+320931.3	-2.38	III	32 \pm 2.5	23 \pm 2.0	16 \pm 1.8	9.8 \pm 1.7	3.8 \pm 0.51	...
391	J034419.25+320734.7	-1.30	II	16 \pm 1.1	14 \pm 1.1	13 \pm 1.0	14 \pm 1.1	8.3 \pm 0.94	...
392	J034420.18+320856.5	-1.66	III	12 \pm 0.90	11 \pm 0.78	9.3 \pm 0.73	9.8 \pm 0.79	6.0 \pm 0.89	...
393	J034421.23+320114.5	-1.39	II	7.3 \pm 0.51	5.3 \pm 0.42	3.9 \pm 0.34	4.0 \pm 0.36	8.9 \pm 0.97	...
394	J034421.29+321237.2	-1.48	II	5.0 \pm 0.39	4.8 \pm 0.34	4.0 \pm 0.32	3.5 \pm 0.32	3.2 \pm 0.42	...
395	J034421.31+321156.3	-1.35	II	14 \pm 1.1	12 \pm 0.88	11 \pm 0.86	14 \pm 0.97	15 \pm 1.6	...
396	J034421.35+315932.6	0.52	0+I	44 \pm 3.0	67 \pm 4.7	79 \pm 5.3	93 \pm 6.5	260 \pm 28	610 \pm 88
397	J034421.57+321509.7	-1.73	III	6.3 \pm 0.47	4.7 \pm 0.38	3.2 \pm 0.35	2.2 \pm 0.33	5.0 \pm 0.66	...
398	J034421.62+321037.7	-1.09	II	75 \pm 5.4	67 \pm 4.8	53 \pm 4.2	50 \pm 4.2	68 \pm 7.2	...
399	J034422.29+320542.8	-0.89	II	41 \pm 2.8	30 \pm 2.5	28 \pm 2.3	40 \pm 2.7	130 \pm 13	...
400	J034422.34+321200.7	-1.13	II	20 \pm 1.5	20 \pm 1.4	21 \pm 1.4	26 \pm 1.7	26 \pm 2.7	...
401	J034422.58+320153.6	-1.05	II	20 \pm 1.4	13 \pm 1.2	10 \pm 1.1	8.7 \pm 1.1	73 \pm 7.6	...
402	J034422.70+320142.3	-1.68	III	4.6 \pm 0.32	3.4 \pm 0.27	2.7 \pm 0.24	2.6 \pm 0.26	7.8 \pm 1.8	...
403	J034423.65+320152.7	-1.36	II	13 \pm 0.91	11 \pm 0.8	9.7 \pm 0.71	11 \pm 0.82	10 \pm 1.2	...
404	J034424.46+320143.7	-1.25	II	2.6 \pm 0.19	2.7 \pm 0.18	2.2 \pm 0.17	2.4 \pm 0.19	4.2 \pm 1.0	...
405	J034424.84+321348.4	1.65	0+I	0.27 \pm 0.02	0.32 \pm 0.02	0.33 \pm 0.07	0.99 \pm 0.21	36 \pm 3.7	...
406	J034425.32+321012.7	-1.42	II	14 \pm 1.1	12 \pm 0.93	11 \pm 0.88	14 \pm 1.0	12 \pm 3.9	...
407	J034425.52+321131.2	-0.79	II	63 \pm 4.8	54 \pm 4.2	46 \pm 3.6	67 \pm 4.4	150 \pm 16	...
408	J034425.55+320617.1	-1.37	II	22 \pm 1.5	16 \pm 0.13	1.3 \pm 1.2	14 \pm 1.4	30 \pm 3.4	...
409	J034425.71+321549.2	-1.06	II	3.1 \pm 0.23	2.7 \pm 0.20	2.4 \pm 0.2	2.7 \pm 0.23	5.9 \pm 0.70	...
410	J034426.04+320430.4	-1.15	II	570 \pm 39	520 \pm 39	450 \pm 33	490 \pm 40	540 \pm 58	...

Table 1
(Continued)

E09 Index	Source Name (SSTc2d +)	α	Class	IRAC ^a 3.6 μm	IRAC 4.5 μm	IRAC 5.8 μm	IRAC 8.0 μm	MIPS ^a 24 μm	MIPS 70 μm
411	J034426.70+320820.3	-1.21	II	47 \pm 3.6	39 \pm 2.9	28 \pm 2.4	31 \pm 2.7	59 \pm 6.4	...
412	J034427.22+322028.8	-1.39	II	4.5 \pm 0.34	3.9 \pm 0.29	3.2 \pm 0.27	3.4 \pm 0.27	4.3 \pm 0.51	...
413	J034427.26+321420.9	-1.17	II	14 \pm 1.1	13 \pm 0.92	11 \pm 0.83	13 \pm 0.92	23 \pm 2.4	...
414	J034427.26+321037.3	-1.60	II	9.7 \pm 0.72	8.3 \pm 0.62	6.1 \pm 0.6	6.4 \pm 0.61	14 \pm 3.5	...
416	J034428.14+321600.2	-2.35	III	14 \pm 1.1	10 \pm 0.85	7.3 \pm 0.75	4.7 \pm 0.72	1.8 \pm 0.32	...
417	J034428.51+315954.0	-1.51	II	23 \pm 1.6	19 \pm 1.5	15 \pm 1.3	16 \pm 1.3	16 \pm 1.7	...
418	J034428.95+320137.9	-1.00	II	18 \pm 1.3	17 \pm 1.2	14 \pm 0.99	17 \pm 1.2	41 \pm 4.4	...
419	J034429.23+320115.7	-1.33	II	11 \pm 0.76	8.0 \pm 0.64	5.9 \pm 0.55	5.8 \pm 0.57	17 \pm 1.8	...
420	J034429.74+321039.8	-1.08	II	53 \pm 4.0	47 \pm 3.4	37 \pm 3.0	45 \pm 3.3	160 \pm 17	...
421	J034429.80+320054.6	-0.93	II	7.8 \pm 0.54	6.9 \pm 0.50	6.8 \pm 0.48	8.2 \pm 0.54	9.9 \pm 0.11	...
422	J034429.98+321922.6	-2.19	III	14 \pm 1.1	11 \pm 0.87	7.0 \pm 0.78	4.2 \pm 0.71	2.2 \pm 0.32	...
423	J034430.14+320118.2	-1.83	III	10 \pm 0.71	7.2 \pm 0.59	5.7 \pm 0.51	5.3 \pm 0.54	3.9 \pm 0.53	...
424	J034430.30+321135.2	0.05	Flat	3.3 \pm 0.24	4.0 \pm 0.27	6.2 \pm 0.41	8.4 \pm 0.66	20 \pm 2.5	...
425	J034430.84+320955.7	-1.46	II	51 \pm 3.7	35 \pm 3.1	41 \pm 3.3	74 \pm 4.8	26 \pm 6.8	...
426	J034431.13+321848.5	-0.92	II	8.6 \pm 0.64	8.5 \pm 0.59	7.8 \pm 0.53	9.8 \pm 0.61	18 \pm 1.9	...
427	J034431.19+320558.9	-0.59	II	13 \pm 0.88	13 \pm 0.94	13 \pm 0.9	13 \pm 0.91	31 \pm 3.3	...
428	J034431.37+320014.2	-1.28	II	69 \pm 5.3	63 \pm 4.7	53 \pm 3.9	67 \pm 4.5	77 \pm 8.1	...
429	J034431.55+320844.9	-2.36	III	42 \pm 3.2	29 \pm 2.5	20 \pm 2.3	13 \pm 2.2	12 \pm 3.8	...
430	J034432.04+321143.7	-0.62	II	200 \pm 16	150 \pm 13	330 \pm 22	1000 \pm 66	430 \pm 45	...
431	J034432.59+320855.7	-1.93	III	23 \pm 1.7	16 \pm 1.4	14 \pm 1.2	13 \pm 1.3	15 \pm 4.0	...
432	J034433.22+321257.4	-1.35	II	6.4 \pm 0.47	4.9 \pm 0.38	4.1 \pm 0.35	4.6 \pm 0.44	7.0 \pm 0.89	...
433	J034433.79+315830.2	-1.25	II	14 \pm 1.0	12 \pm 0.88	9.2 \pm 0.77	9.7 \pm 0.80	24 \pm 2.5	...
434	J034434.05+320657.0	-0.81	II	4.6 \pm 0.32	4.3 \pm 0.32	4.5 \pm 0.32	5.5 \pm 0.40	5.6 \pm 1.3	...
435	J034434.14+321635.7	-1.20	II	6.0 \pm 0.45	5.3 \pm 0.39	4.5 \pm 0.37	5.0 \pm 0.39	7.9 \pm 0.94	...
436	J034434.21+320946.3	-2.02	III	620 \pm 54	380 \pm 39	300 \pm 35	170 \pm 32	350 \pm 53	...
437	J034434.29+321240.7	-1.34	II	29 \pm 2.2	29 \pm 2.0	23 \pm 1.6	27 \pm 1.8	30 \pm 3.2	...
438	J034434.69+321600.1	-0.43	II	17 \pm 1.3	19 \pm 1.2	18 \pm 1.1	21 \pm 1.3	150 \pm 15	...
439	J034434.71+321554.4	-1.98	III	12 \pm 0.96	9.3 \pm 0.74	6.3 \pm 0.64	3.6 \pm 0.62	7.2 \pm 1.4	...
440	J034434.81+315655.2	-1.19	II	13 \pm 0.94	10 \pm 0.82	7.4 \pm 0.73	5.9 \pm 0.71	23 \pm 2.5	...
441	J034434.99+321531.1	-1.29	II	10 \pm 0.78	9.8 \pm 0.69	9.1 \pm 0.67	12 \pm 0.77	8.6 \pm 0.94	...
443	J034435.38+320736.2	-1.20	II	37 \pm 2.7	38 \pm 2.7	30 \pm 2.2	46 \pm 2.9	55 \pm 5.8	...
444	J034435.38+321004.6	-1.57	II	430 \pm 37	350 \pm 32	290 \pm 26	300 \pm 27	270 \pm 30	...
445	J034435.47+320856.3	-1.13	II	12 \pm 0.90	10 \pm 0.78	9.3 \pm 0.79	11 \pm 1.2	50 \pm 11	...
446	J034435.69+320303.5	-1.06	II	21 \pm 1.5	19 \pm 1.4	18 \pm 1.3	22 \pm 0.14	27 \pm 3.1	...
448	J034436.96+320645.2	-1.93	III	230 \pm 15	160 \pm 14	130 \pm 13	98 \pm 12	47 \pm 5.3	...
449	J034437.40+321224.2	-0.93	II	21 \pm 1.5	16 \pm 1.3	12 \pm 1.1	15 \pm 1.3	77 \pm 8.2	...
450	J034437.88+320804.1	-1.22	II	97 \pm 6.8	93 \pm 6.5	68 \pm 5.4	87 \pm 6.2	100 \pm 11	...
451	J034437.98+320329.7	-1.24	II	70 \pm 4.8	60 \pm 4.6	51 \pm 4.0	72 \pm 4.7	75 \pm 8.1	...
452	J034438.01+321137.0	-1.49	II	8.2 \pm 0.6	6.5 \pm 0.51	6.0 \pm 0.5	7.0 \pm 0.61	10 \pm 2.9	...
453	J034438.46+320735.7	-1.13	II	55 \pm 3.8	44 \pm 3.5	44 \pm 3.3	73 \pm 4.6	88 \pm 9.4	...
454	J034438.54+320800.6	-0.97	II	36 \pm 2.5	29 \pm 2.3	23 \pm 2.0	35 \pm 2.6	120 \pm 13	...
455	J034438.97+320319.7	-1.25	II	4.1 \pm 0.29	3.4 \pm 0.26	2.9 \pm 0.25	3.8 \pm 0.37	5.9 \pm 1.6	...
456	J034439.19+322008.9	-1.80	III	13 \pm 0.95	10 \pm 0.80	8.6 \pm 0.75	8.3 \pm 0.81	6.2 \pm 1.8	...
457	J034439.21+320944.8	-1.44	II	22 \pm 1.6	19 \pm 1.4	16 \pm 1.4	18 \pm 1.6	52 \pm 15	...
458	J034439.80+321804.0	-1.40	II	27 \pm 2.0	21 \pm 1.7	17 \pm 1.5	18 \pm 1.5	24 \pm 2.5	...
459	J034441.74+321202.2	-1.07	II	15 \pm 1.1	11 \pm 0.88	8.6 \pm 0.81	8.9 \pm 0.85	56 \pm 5.9	...
460	J034442.04+320859.9	-2.01	III	41 \pm 3.2	34 \pm 2.6	25 \pm 2.4	26 \pm 2.6	17 \pm 4.0	...
461	J034442.15+320902.1	-0.52	II	26 \pm 2.2	35 \pm 2.2	36 \pm 2.2	39 \pm 2.4	74 \pm 7.8	...
462	J034442.58+321002.5	-1.29	II	14 \pm 1.1	14 \pm 0.99	13 \pm 0.91	14 \pm 1.0	16 \pm 2.5	...
463	J034442.76+320833.7	-1.35	II	14 \pm 1.0	12 \pm 0.91	12 \pm 0.89	13 \pm 1.1	15 \pm 3.4	...
464	J034443.03+321559.6	-0.65	II	5.4 \pm 0.39	5.1 \pm 0.36	5.0 \pm 0.37	7.9 \pm 0.49	20 \pm 2.1	...
466	J034443.32+320131.5	0.61	0+I	260 \pm 19	400 \pm 27	480 \pm 25	740 \pm 38	2300 \pm 250	...
467	J034443.53+320742.7	-1.97	III	36 \pm 2.6	23 \pm 2.0	16 \pm 1.8	11 \pm 1.9	11 \pm 1.5	...
468	J034443.78+321030.4	-0.87	II	24 \pm 1.7	23 \pm 1.6	24 \pm 1.6	43 \pm 2.4	74 \pm 7.9	...
469	J034443.96+320136.2	0.74	0+I	3.9 \pm 0.30	8.5 \pm 0.89	7.0 \pm 0.41	...	170 \pm 23	11000 \pm 1200
470	J034444.59+320812.5	-0.91	II	33 \pm 2.3	32 \pm 2.2	27 \pm 2.0	39 \pm 2.4	30 \pm 4.0	...
471	J034444.72+320402.5	-1.18	II	130 \pm 9.1	120 \pm 8.8	100 \pm 7.7	120 \pm 8.4	170 \pm 18	...
472	J034445.20+320119.6	-0.58	II	18 \pm 1.2	17 \pm 1.2	19 \pm 1.1	23 \pm 1.3	35 \pm 3.8	...
473	J034450.35+315236.0	-1.12	II	4.0 \pm 0.28	3.7 \pm 0.26	3.0 \pm 0.24	3.0 \pm 0.24	5.2 \pm 0.57	...
475	J034452.05+315825.2	-1.27	II	16 \pm 1.1	1.4 \pm 0.99	11 \pm 0.89	9.9 \pm 0.87	15 \pm 1.5	...
476	J034455.62+320919.8	-2.23	III	33 \pm 2.3	22 \pm 1.9	14 \pm 1.6	9.2 \pm 1.5	10 \pm 2.3	...
477	J034456.14+320915.2	-1.12	II	110 \pm 7.8	79 \pm 6.7	65 \pm 6.0	53 \pm 5.8	230 \pm 25	...
478	J034456.84+315411.4	-1.35	II	3.0 \pm 0.2	2.2 \pm 0.18	1.7 \pm 0.16	1.2 \pm 0.17	3.3 \pm 0.39	...

Table 1
(Continued)

E09 Index	Source Name (SSTc2d +)	α	Class	IRAC ^a 3.6 μm	IRAC 4.5 μm	IRAC 5.8 μm	IRAC 8.0 μm	MIPS ^a 24 μm	MIPS 70 μm
479	J034456.90+322035.6	-0.72	II	2.9 \pm 0.21	3.1 \pm 0.19	2.7 \pm 0.18	2.5 \pm 0.21	6.3 \pm 0.80	...
480	J034457.72+320741.7	-1.10	II	3.1 \pm 0.21	2.3 \pm 0.18	1.7 \pm 0.17	1.4 \pm 0.2	6.9 \pm 0.8	...
481	J034457.85+320401.5	-1.82	III	4.9 \pm 0.33	3.8 \pm 0.30	3.0 \pm 0.28	3.2 \pm 0.29	1.6 \pm 0.35	...
482	J034458.55+315827.1	-1.19	II	2.3 \pm 0.16	2.0 \pm 0.15	1.8 \pm 0.13	2.2 \pm 0.15	1.7 \pm 0.30	...
483	J034459.85+321331.9	-1.68	III	6.6 \pm 0.46	5.2 \pm 0.41	4.4 \pm 0.39	4.4 \pm 0.41	2.3 \pm 0.37	...
484	J034500.45+320320.1	-1.78	III	5.3 \pm 0.37	4.1 \pm 0.32	3.2 \pm 0.28	2.5 \pm 0.28	2.1 \pm 0.38	...
485	J034501.43+320501.7	-2.31	III	44 \pm 3.0	30 \pm 2.6	20 \pm 2.4	14 \pm 2.3	4.4 \pm 0.51	...
486	J034504.66+321501.1	-2.10	III	10 \pm 0.75	7.3 \pm 0.60	5.3 \pm 0.53	4.4 \pm 0.52	2.5 \pm 0.82	...
487	J034507.64+321027.9	-2.48	III	40 \pm 3.5	34 \pm 2.6	24 \pm 2.3	15 \pm 2.1	3.9 \pm 0.49	...
488	J034513.08+322005.3	-1.48	II	2.6 \pm 0.2	2.4 \pm 0.17	1.9 \pm 0.15	2.1 \pm 0.17	1.7 \pm 0.27	...
490	J034513.82+321210.0	0.43	0+I	2.9 \pm 0.2	4.7 \pm 0.27	8.1 \pm 0.42	16 \pm 0.76	69 \pm 7.4	290 \pm 38
491	J034516.34+320620.1	-0.71	II	240 \pm 17	280 \pm 18	260 \pm 16	370 \pm 24	450 \pm 48	470 \pm 59
492	J034517.82+321205.8	-1.52	II	6.3 \pm 0.47	5.5 \pm 0.41	4.2 \pm 0.38	4.0 \pm 0.36	4.3 \pm 0.53	...
493	J034520.46+320634.5	-1.13	II	130 \pm 8.9	120 \pm 8.4	91 \pm 7.2	110 \pm 7.9	230 \pm 24	370 \pm 42
494	J034525.15+320930.3	-0.83	II	41 \pm 2.7	35 \pm 2.6	31 \pm 2.4	47 \pm 2.9	120 \pm 12	91 \pm 16
495	J034529.72+315919.7	-1.29	II	4.6 \pm 0.31	3.6 \pm 0.27	3.2 \pm 0.26	3.3 \pm 0.27	5.1 \pm 0.58	...
497	J034535.64+315954.4	-1.32	II	12 \pm 0.81	9.4 \pm 0.71	8.1 \pm 0.65	9.9 \pm 0.71	14 \pm 1.5	...

Note.

^a *Spitzer* flux densities in mJy.

(This table is available in machine-readable and Virtual Observatory (VO) forms.)

L1455, associated with the Perseus cloud complex. Figure 1 displays the boundaries of these two cluster regions in red. The NGC 1333 region was defined from 03^h28^m00^s to 03^h30^m00^s in R.A. and +31°06′00″ to +31°30′00″ in decl. The IC 348 region runs from 03^h43^m12^s to 03^h46^m00^s in R.A. and +31°48′00″ to +32°24′00″ in decl. The RC includes all of the IRAC observation area (dashed outline in Figure 1) outside of the cluster boundaries.

These three regions were previously defined in Jørgensen et al. (2006) and Rebull et al. (2007) based on the boundaries of the GTO observations of the clusters (Lada et al. 2006; Gutermuth et al. 2008). The regions do not represent physical boundaries of the clusters, but reflect *Spitzer*’s mapping footprint. Therefore, the IC 348 and NGC 1333 regions may include some YSOs that are not physically associated with the clusters. However, for consistency within this series of papers, we maintain these somewhat arbitrary boundaries.

Figure 5 is a histogram of the number of identified sources with infrared flux versus the “probability” of being a background galaxy. Sources with low probabilities were considered YSO candidates. The cutoff to separate YSOs and galaxies in terms of probability is $\log P \leq -1.47$ (as in Harvey et al. 2007). There is a small tail of sources found in Perseus between $\log P = -1.5$ and -2.0 . Harvey et al. (2007) predicted no more than zero to one contaminant galaxies in this tail based on comparisons with the SWIRE catalog. Most of the extragalactic sources appear in the RC histogram rather than being associated with the young clusters in Perseus because of their uniform spacing over the cloud area.

Previous papers in this series have reported the number of YSO candidates (YSOc) in a given c2d cloud. However, in recent years, the c2d YSOc lists have been used and refined in a number of studies (e.g., E09, Dunham et al. 2013). In the course of these studies, all of the YSOc were visually inspected to eliminate resolved galaxies and artifacts (E09). Therefore, following the terminology in E09, the “candidate” designation

has been dropped for this study and we will discuss the YSOs found in Perseus.

Using the described selection method, we identified 385 YSOs in Perseus. IRAC and MIPS fluxes for these sources, as well as the YSOs in the other c2d clouds, were published in online tables as part of a paper summarizing the c2d *Spitzer* Legacy project results (E09). The tables also provide additional spectral energy distribution (SED) data, classifications, and derived properties, such as bolometric temperature and luminosity, for all of the Perseus YSOs. Dunham et al. (2013) updated the SEDs and other properties of the protostellar population in Perseus.

Recently, Hsieh & Lai (2013) developed a new method for separating YSOs and galaxies in *Spitzer* data sets using multi-dimensional (multi-D) magnitude space. They analyzed all of the c2d clouds with this new method, adding 100 YSO candidates and removing 16 YSOs in Perseus compared to the E09 c2d list for a total of 469 YSOc in Perseus. Figure 6 shows the location of the Hsieh & Lai (2013) new YSO candidates on the 8 μm map of the cloud. Sixteen c2d-identified YSOs were not included by Hsieh & Lai (2013) for various reasons (see also their Table 5): six are jet knots, six appear to be confused with nearby sources or cloud structures, three were not identified as high reliability sources by c2d, and one was identified by the multi-D process as a giant star. We agree with Hsieh & Lai’s characterization of these 16 sources and have removed them from our list of YSOs in Perseus.

The multi-D method developed for identifying YSO candidates by Hsieh & Lai (2013) is relatively new and completely different from the established c2d method presented in previous papers in this series and in other works by the c2d team. Because our method, as described above, does not identify the 100 additional sources in the Hsieh & Lai (2013) candidate list as YSOs and for consistency with the previous work from the c2d team, we do not include the new Hsieh & Lai (2013) YSO candidates. The Hsieh & Lai (2013)

Table 2
YSOs in the NGC 1333 Region

E09 Index	Source Name (SSTc2d +)	α	Class	IRAC ^a 3.6 μm	IRAC 4.5 μm	IRAC 5.8 μm	IRAC 8.0 μm	MIPS ^a 24 μm	MIPS 70 μm
136	J032832.56+311105.1	0.51	0+I	1.4 \pm 0.13	3.1 \pm 0.23	3.3 \pm 0.23	5.3 \pm 0.37	63 \pm 6.7	63 \pm 6.7
138	J032834.49+310051.1	0.31	0+I	6.6 \pm 0.46	16 \pm 0.86	31 \pm 1.5	45 \pm 2.2	69 \pm 7.4	160 \pm 19
141	J032837.09+311330.8	1.93	0+I	43 \pm 3.3	120 \pm 7.7	340 \pm 17	950 \pm 54	7900 \pm 1400	55000 \pm 5800
142	J032838.78+311806.6	-0.25	Flat	6.5 \pm 0.46	9.4 \pm 0.58	10 \pm 0.59	13 \pm 0.70	18 \pm 2.0	...
143	J032839.10+310601.7	1.55	0+I	0.19 \pm 0	0.36 \pm 0.03	0.55 \pm 0.05	1.2 \pm 0.09	28 \pm 3.0	96 \pm 15
144	J032839.71+311731.9	0.61	0+I	19 \pm 1.4	31 \pm 1.8	41 \pm 2.2	55 \pm 2.8	220 \pm 22	370 \pm 41
145	J032840.63+311756.5	0.96	0+I	0.04 \pm 0.01	0.26 \pm 0.02	0.62 \pm 0.05	1.2 \pm 0.08	6.0 \pm 0.69	...
147	J032843.24+311042.7	-1.86	III	23 \pm 1.6	16 \pm 1.3	13 \pm 1.1	11 \pm 1.1	5.8 \pm 0.66	...
148	J032843.28+311732.9	0.24	Flat	260 \pm 20	470 \pm 28	620 \pm 38	1000 \pm 61	2200 \pm 240	2100 \pm 240
149	J032844.09+312052.7	-1.34	II	6.4 \pm 0.47	5.2 \pm 0.41	4.7 \pm 0.37	5.2 \pm 0.39	4.8 \pm 0.53	...
151	J032846.21+311638.4	-1.84	III	51 \pm 4.0	43 \pm 3.3	38 \pm 3.1	36 \pm 3.0	15 \pm 1.6	...
152	J032847.65+312406.0	-1.32	II	35 \pm 2.7	29 \pm 2.1	25 \pm 1.9	20 \pm 1.9	21 \pm 2.1	...
153	J032847.84+311655.1	-1.10	II	39 \pm 3.0	46 \pm 3.1	38 \pm 2.5	43 \pm 2.7	53 \pm 5.6	...
154	J032848.77+311608.8	0.20	Flat	2.3 \pm 0.17	3.1 \pm 0.19	4.3 \pm 0.24	7.2 \pm 0.37	22 \pm 2.3	...
156	J032850.62+304244.7	-0.95	II	220 \pm 19	200 \pm 16	180 \pm 15	270 \pm 22	390 \pm 40	...
157	J032851.08+311632.4	-1.48	II	6.3 \pm 0.49	5.6 \pm 0.42	5.1 \pm 0.4	5.8 \pm 0.42	4.0 \pm 0.49	...
158	J032851.20+311954.8	-1.00	II	78 \pm 5.8	72 \pm 5.2	69 \pm 4.9	110 \pm 6.4	150 \pm 16	...
159	J032851.26+311739.3	0.60	0+I	0.96 \pm 0.08	1.6 \pm 0.10	2.2 \pm 0.01	6.5 \pm 0.42	29 \pm 3.0	...
160	J032852.15+311547.1	-1.34	II	8.8 \pm 0.65	7.3 \pm 0.56	6.6 \pm 0.53	8.1 \pm 0.58	5.3 \pm 0.62	...
162	J032852.17+312245.3	-1.45	II	27 \pm 2.1	22 \pm 1.8	19 \pm 1.6	22 \pm 1.6	25 \pm 2.6	...
163	J032852.92+311626.4	-1.49	II	4.8 \pm 0.37	4.2 \pm 0.32	3.8 \pm 0.3	3.9 \pm 0.31	3.2 \pm 0.46	...
164	J032853.96+311809.3	-1.29	II	69 \pm 5.3	60 \pm 4.2	51 \pm 3.6	70 \pm 4.4	130 \pm 13	350 \pm 47
165	J032854.09+311654.2	-1.07	II	15 \pm 1.1	12 \pm 0.91	11 \pm 0.9	16 \pm 1.0	23 \pm 2.7	...
166	J032854.63+311651.1	-1.08	II	94 \pm 7.1	85 \pm 6.2	80 \pm 5.5	110 \pm 6.6	140 \pm 14	...
167	J032855.08+311628.7	-0.76	II	140 \pm 9.9	120 \pm 8.8	110 \pm 7.7	130 \pm 8.9	250 \pm 26	...
168	J032855.55+311436.7	2.39	0+I	1.4 \pm 0.12	17 \pm 1.2	29 \pm 1.8	41 \pm 2.8	...	140000 \pm 15000
169	J032856.12+311908.4	-0.51	II	8.5 \pm 0.62	25 \pm 1.6	34 \pm 1.7	34 \pm 1.7	24 \pm 2.6	...
170	J032856.32+312227.9	-0.40	II	23 \pm 1.7	24 \pm 1.6	29 \pm 1.8	41 \pm 2.2	100 \pm 11	560 \pm 72
171	J032856.60+310737.0	0.01	Flat	1.1 \pm 0.09	3.4 \pm 0.22	2.5 \pm 0.17	0.87 \pm 0.11	14 \pm 1.4	110 \pm 14
172	J032856.65+311835.5	-1.14	II	150 \pm 11	130 \pm 10	90 \pm 7.5	100 \pm 8.1	280 \pm 29	650 \pm 76
173	J032856.97+311622.3	-0.74	II	24 \pm 1.9	20 \pm 1.6	17 \pm 1.4	26 \pm 1.7	210 \pm 22	...
174	J032857.18+311534.6	-0.71	II	5.1 \pm 0.40	4.8 \pm 0.35	5.3 \pm 0.37	8.2 \pm 0.45	16 \pm 1.7	...
175	J032857.21+311419.1	1.40	0+I	46 \pm 3.2	130 \pm 8.1	330 \pm 17	500 \pm 30	5000 \pm 530	31000 \pm 3300
177	J032857.70+311948.1	-0.96	II	19 \pm 1.5	19 \pm 1.3	18 \pm 1.2	26 \pm 1.6	41 \pm 4.4	...
178	J032858.11+311803.7	-2.37	III	12 \pm 0.92	8.7 \pm 0.74	6.3 \pm 0.66	4.7 \pm 0.64	1.3 \pm 0.28	...
179	J032858.26+312209.2	-0.99	II	5.3 \pm 0.38	4.9 \pm 0.38	4.5 \pm 0.34	5.7 \pm 1.1	44 \pm 12	...
180	J032858.27+312202.0	-1.07	II	13 \pm 1.0	14 \pm 0.9	13 \pm 0.87	17 \pm 0.99	19 \pm 4.1	...
181	J032858.43+312217.5	0.82	0+I	57 \pm 4.3	110 \pm 11	230 \pm 12	340 \pm 21	990 \pm 110	950 \pm 110
182	J032859.23+312032.5	-0.02	Flat	0.90 \pm 0.10	2.0 \pm 0.19	1.7 \pm 0.17	1.7 \pm 0.24	13 \pm 2.3	...
183	J032859.32+311548.7	-0.08	Flat	160 \pm 11	160 \pm 12	150 \pm 11	250 \pm 14	970 \pm 100	...
184	J032859.56+312146.7	-1.11	II	120 \pm 9.0	120 \pm 8.1	96 \pm 6.8	110 \pm 7.4	12 \pm 13	...
185	J032900.55+311200.8	1.96	0+I	...	0.12 \pm 0	0.14 \pm 0.04	...	17 \pm 1.8	1300 \pm 180
186	J032901.56+312020.6	2.30	0+I	770 \pm 66	1500 \pm 110	2200 \pm 270	4100 \pm 250	...	24000 \pm 2600
188	J032902.81+312217.2	-1.32	II	9.5 \pm 0.72	9.1 \pm 0.61	8.5 \pm 0.57	9.6 \pm 0.62	7.9 \pm 2.1	...
189	J032903.15+312238.0	-0.76	II	35 \pm 2.5	38 \pm 2.5	35 \pm 2.3	52 \pm 3.0	100 \pm 11	...
190	J032903.22+312545.1	-0.81	II	2.6 \pm 0.19	2.3 \pm 0.18	2.1 \pm 0.17	2.4 \pm 0.19	9.2 \pm 1.0	...
191	J032903.33+312314.6	1.00	0+I	6.5 \pm 0.47	10 \pm 0.59	24 \pm 1.2	61 \pm 2.9	160 \pm 17	...
192	J032903.78+311603.8	0.85	0+I	1300 \pm 100	480 \pm 110	3600 \pm 420	7500 \pm 430	...	130000 \pm 13000
194	J032903.87+312148.6	-1.06	II	260 \pm 20	230 \pm 18	210 \pm 15	280 \pm 19	320 \pm 34	...
195	J032904.06+311446.5	1.32	0+I	0.63 \pm 0.05	1.5 \pm 0.12	1.7 \pm 0.10	1.8 \pm 0.12	83 \pm 8.8	...
198	J032904.68+311659.0	-0.46	II	11 \pm 0.83	12 \pm 0.78	12 \pm 0.79	20 \pm 1.1	41 \pm 4.5	...
199	J032904.73+311134.9	-0.62	II	14 \pm 0.94	17 \pm 1.1	16 \pm 0.89	19 \pm 1.1	17 \pm 1.8	...
200	J032904.95+312038.4	0.06	Flat	13 \pm 0.95	16 \pm 1.0	19 \pm 1.1	28 \pm 1.5	110 \pm 12	...
201	J032905.18+312036.9	-0.98	II	2.9 \pm 0.27	4.3 \pm 0.27	5.3 \pm 0.34	7.8 \pm 0.42	38 \pm 6.0	...
202	J032905.78+311639.6	-1.08	II	470 \pm 37	460 \pm 33	410 \pm 27	500 \pm 30	450 \pm 48	...
204	J032906.33+311346.4	-1.14	II	48 \pm 3.4	47 \pm 3.1	43 \pm 2.5	52 \pm 3.1	55 \pm 5.9	...
205	J032907.78+312157.3	2.30	0+I	1000 \pm 110	2400 \pm 230	3900 \pm 360	3400 \pm 330	...	50000 \pm 5300
206	J032907.96+312251.4	-1.16	II	130 \pm 10	120 \pm 8.6	120 \pm 8.0	160 \pm 13	110 \pm 31	...
207	J032908.97+312256.1	-0.21	Flat	43 \pm 3.2	54 \pm 3.5	56 \pm 4.6	75 \pm 16	140 \pm 31	...
208	J032909.10+312305.5	-0.33	II	22 \pm 1.6	23 \pm 1.5	23 \pm 2.9	70 \pm 16	240 \pm 46	...
209	J032909.10+312128.7	1.05	0+I	39 \pm 3.3	110 \pm 6.9	170 \pm 9.8	170 \pm 13	430 \pm 63	...
210	J032909.34+312104.1	-0.51	II	5.9 \pm 0.44	4.7 \pm 0.38	5.1 \pm 0.50	8.6 \pm 0.76	41 \pm 5.6	...
211	J032909.40+311413.8	-0.87	II	2.9 \pm 0.20	7.3 \pm 0.51	8.9 \pm 0.45	6.0 \pm 0.35	3.6 \pm 0.50	...

Table 2
(Continued)

E09 Index	Source Name (SSTc2d +)	α	Class	IRAC ^a 3.6 μm	IRAC 4.5 μm	IRAC 5.8 μm	IRAC 8.0 μm	MIPS ^a 24 μm	MIPS 70 μm
212	J032909.49+312720.9	-1.10	II	5.2 ± 0.39	4.7 ± 0.35	4.2 ± 0.32	6.0 ± 0.39	7.4 ± 0.85	...
213	J032909.65+312256.3	-1.60	II	96 ± 6.9	68 ± 5.7	56 ± 6.0	87 ± 16	120 ± 29	...
214	J032910.47+312334.7	-1.41	II	10 ± 0.72	8.9 ± 0.62	8.3 ± 0.60	9.5 ± 0.87	13 ± 3.3	...
215	J032910.49+311331.0	2.49	0+I	...	0.11 ± 0.01	0.17 ± 0.03	...	37 ± 3.9	34000 ± 3600
216	J032910.65+311340.0	0.42	0+I	0.07 ± 0.01	1.3 ± 0.08	0.74 ± 0.05	0.37 ± 0.06	5.5 ± 0.92	...
217	J032910.68+311820.6	1.84	0+I	2.6 ± 0.26	9.0 ± 0.89	13 ± 1.1	14 ± 1.0	890 ± 94	21000 ± 2300
218	J032910.84+311642.6	-0.32	II	8.0 ± 0.65	10 ± 0.69	13 ± 0.76	22 ± 1.2	28 ± 2.9	...
220	J032911.26+311831.4	1.79	0+I	1.0 ± 0.11	5.2 ± 0.35	6.4 ± 0.42	5.4 ± 0.36	600 ± 63	...
221	J032911.89+312127.0	0.32	0+I	23 ± 1.7	34 ± 2.0	41 ± 2.5	51 ± 4.0	60 ± 20	...
222	J032912.06+311305.4	0.85	0+I	0.04 ± 0.01	1.3 ± 0.09	0.80 ± 0.05	0.39 ± 0.11	21 ± 2.9	12000 ± 1300
223	J032912.06+311301.7	0.07	Flat	0.98 ± 0.07	17 ± 0.91	6.2 ± 0.32	4.5 ± 0.28	44 ± 4.6	...
224	J032912.97+311814.3	1.56	0+I	66 ± 5.2	240 ± 13	340 ± 18	420 ± 24	850 ± 89	4400 ± 470
225	J032913.14+312252.8	-1.33	II	140 ± 11	140 ± 9.3	120 ± 8.1	120 ± 8.4	77 ± 8.3	...
226	J032913.54+311358.2	2.50	0+I	0.04 ± 0	...	0.32 ± 0.05	...	32 ± 3.5	4000 ± 550
227	J032914.40+311444.1	-0.70	II	4.4 ± 0.35	16 ± 1.5	8.1 ± 0.65	6.7 ± 0.50	12 ± 1.3	...
228	J032916.61+312349.4	-1.18	II	32 ± 2.3	31 ± 2.1	32 ± 2.1	43 ± 2.5	21 ± 3.1	...
229	J032916.69+311618.2	-2.43	III	24 ± 1.7	17 ± 1.5	12 ± 1.3	7.2 ± 1.3	1.9 ± 0.31	...
230	J032916.83+312325.1	-0.57	II	3.0 ± 0.22	2.7 ± 0.20	2.9 ± 0.22	4.2 ± 0.25	23 ± 2.7	...
231	J032917.17+312746.5	1.69	0+I	0.6 ± 0.06	1.6 ± 0.16	1.5 ± 0.13	1.1 ± 0.14	130 ± 14	2000 ± 300
233	J032917.68+312245.0	-0.94	II	450 ± 34	430 ± 31	490 ± 33	520 ± 36	580 ± 61	...
234	J032917.78+311948.0	-1.23	II	5.2 ± 0.38	4.5 ± 0.33	3.9 ± 0.31	4.4 ± 0.33	5.5 ± 0.61	...
235	J032918.26+312319.9	1.09	0+I	1.3 ± 0.10	3.8 ± 0.2	8.0 ± 0.38	14 ± 0.72	68 ± 7.7	...
236	J032918.67+312017.7	0.16	Flat	1.6 ± 0.12	1.8 ± 0.11	1.8 ± 0.13	3.6 ± 0.21	25 ± 2.7	...
237	J032918.74+312325.4	-0.66	II	52 ± 4.0	56 ± 3.9	67 ± 3.9	120 ± 7.0	210 ± 23	...
238	J032920.06+312407.5	0.34	0+I	43 ± 3.4	59 ± 3.6	76 ± 5.0	120 ± 9.9	430 ± 45	...
239	J032920.44+311834.2	-0.25	Flat	130 ± 11	160 ± 10	150 ± 9.4	210 ± 12	510 ± 54	210 ± 30
240	J032921.57+312110.3	-1.24	II	12 ± 0.88	1.1 ± 0.80	9.2 ± 0.75	11 ± 0.80	16 ± 1.8	...
241	J032921.87+311536.2	-1.34	II	120 ± 8.4	120 ± 8.3	87 ± 6.8	93 ± 7.2	95 ± 9.9	...
242	J032923.17+312030.2	-1.03	II	19 ± 1.5	18 ± 1.3	15 ± 1.2	20 ± 1.3	31 ± 3.3	...
243	J032923.25+312653.1	-1.17	II	8.5 ± 0.65	8.5 ± 0.59	7.7 ± 0.55	8.9 ± 0.59	7.6 ± 0.84	...
245	J032924.09+311957.6	-0.13	Flat	3.0 ± 0.22	2.7 ± 0.19	2.7 ± 0.20	4.6 ± 0.26	77 ± 8.2	...
246	J032925.93+312640.1	-0.93	II	100 ± 8.7	120 ± 8.2	140 ± 8.4	210 ± 13	150 ± 16	...
247	J032926.81+312647.6	-1.81	III	53 ± 4.0	35 ± 3.3	25 ± 2.9	19 ± 2.8	20 ± 2.1	...
249	J032929.27+311834.7	-0.98	II	18 ± 1.4	12 ± 1.1	9.1 ± 0.93	8.5 ± 0.93	110 ± 11	290 ± 34
250	J032929.80+312102.6	-1.15	II	18 ± 1.4	14 ± 1.1	15 ± 1.1	21 ± 1.3	31 ± 3.3	...
251	J032930.40+311903.3	-1.11	II	18 ± 1.3	17 ± 1.3	17 ± 1.2	20 ± 1.3	29 ± 3.1	120 ± 29
252	J032932.57+312436.9	-1.22	II	27 ± 2.0	24 ± 1.7	18 ± 1.5	19 ± 1.5	21 ± 2.2	...
253	J032932.88+312712.6	-1.58	II	6.3 ± 0.48	5.2 ± 0.41	4.4 ± 0.37	4.2 ± 0.38	2.6 ± 0.31	...
254	J032937.73+312202.5	-0.97	II	3.7 ± 0.26	3.0 ± 0.23	2.6 ± 0.22	3.2 ± 0.24	7.9 ± 0.87	...
255	J032944.16+311947.3	-0.76	II	1.8 ± 0.13	2.4 ± 0.16	2.4 ± 0.15	2.6 ± 0.15	2.1 ± 0.28	...
258	J032954.04+312052.9	-0.87	II	34 ± 2.6	34 ± 2.3	31 ± 2.2	39 ± 2.4	120 ± 13	200 ± 22

Note.^a *Spitzer* flux densities in mJy.

(This table is available in machine-readable and Virtual Observatory (VO) forms.)

candidates likely include previously unidentified YSOs in Perseus. However, we suggest further observations, such as optical spectra or maps of the molecular cores, are needed to confirm the classification of these faint sources and rule out possibility that the candidates are reddened AGB stars or background galaxies. Therefore, we present 369 YSOs identified by the c2d method (385 from E09 minus 16 excluded by Hsieh & Lai 2013) in Perseus.

E09 calculated the star formation rate (SFR) for all of the c2d clouds based on the number of YSOs (N_{YSO}) identified in each cloud. Assuming a mean mass per YSO of $0.5 M_{\odot}$ and a period of star formation of 2 Myr, E09 report an SFR in Perseus of $96 M_{\odot} \text{ Myr}^{-1}$. With 369 instead of 385 YSOs and a slightly lower SFR of $92 M_{\odot} \text{ Myr}^{-1}$, Perseus maintains the highest SFR among the c2d team's molecular clouds. If all of the YSO

candidates from Hsieh & Lai (2013) are included, the SFR in Perseus increases to $117 M_{\odot} \text{ Myr}^{-1}$.

Figure 6 shows the distribution of the 369 YSOs identified in Perseus. YSOs are found in groups and clusters associated with known regions of star formation. We list and identify the YSOs in each cluster region and the RC. Tables 1 and 2 list the 143 YSOs in the IC 348 region and 104 YSOs in the NGC 1333 region respectively. Table 3 identifies 122 YSOs in the RC.

4. YSO CLASSIFICATION

All of the YSOs identified in the c2d molecular cloud survey with sufficient data were placed in one of four classes according to their spectral index, α : Class 0+I, Flat (i.e., flat-spectrum), Class II, and Class III. We have reclassified the YSOs in Perseus according to an updated spectral index.

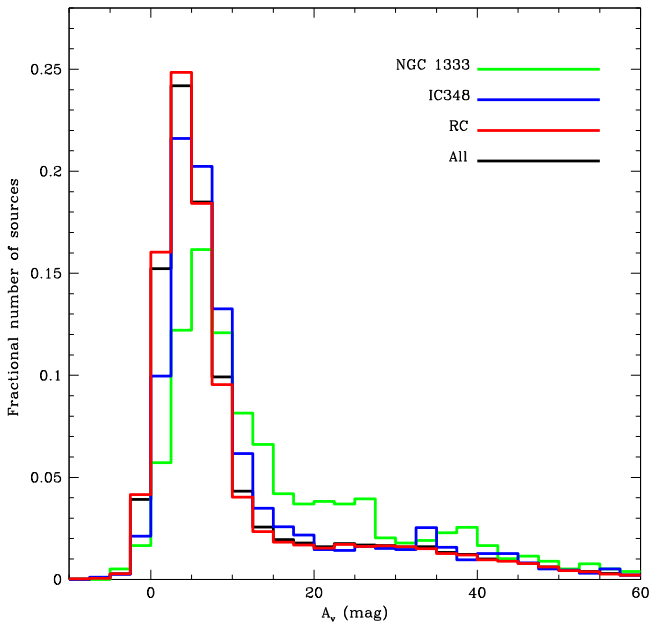


Figure 3. Distribution of the visual extinctions found toward the sources classified as stars in Perseus observed with both IRAC and MIPS. The black line is the distribution toward all stars. The distributions for stars toward NGC 1333, IC 348, and the RC are shown as green, blue, and red lines respectively.

Therefore, some sources are classified differently in this work than in E09.

The spectral index is defined by a least squares fit to the photometry of the source between 2 and 24 μm according to Equation (1) in E09. The near-infrared flux data are from 2MASS. We follow the class definitions of Greene et al. (1994), where $\alpha \geq 0.3$ is a Class I, $-0.3 \leq \alpha < 0.3$ is a Flat source, $-1.6 \leq \alpha < -0.3$ is a Class II, and $\alpha < -1.6$ is a Class III.

Because Greene et al. (1994) do not distinguish between Class 0 and Class I sources and the classes cannot be separated based on spectral index (Dunham et al. 2014, 2015), we classify all sources with $\alpha \geq 0.3$ as Class 0+I. In addition, the Greene et al. (1994) classification scheme does not put a lower limit on α for Class III sources and therefore includes YSOs with spectral energy distributions that resemble bare stellar photospheres. As noted by Gutermuth et al. (2009), *Spitzer* data alone cannot identify diskless Class III sources with no infrared excess. Therefore, our Class III census represents a lower limit for Perseus.

Evans et al. (2009) corrected the c2d large cloud photometry for extinction. Using a mean extinction of $A_v = 5.92$ in Perseus, E09 classified their 385 YSO candidates: 76 Class 0+I, 35 Flat, 244 Class II, and 30 Class III. Following E09, we assign extinction values to all YSOs as follows:

1. We adopt extinction values from the literature for Class II and III YSOs (classified via infrared spectral index; see E09 for details) included in published optical studies.
2. We de-redden the remaining Class II and III YSOs to the intrinsic near-infrared colors of an assumed spectral type of K7, found to be fairly representative of the majority of Class II and III YSOs in the c2d clouds (Oliveira et al. 2009, 2010; see also E09 for details).
3. We de-redden all of the Class 0+I and Flat spectrum YSOs (again classified via infrared spectral index) using

the mean extinction toward all Class II YSOs in Perseus ($A_v = 5.9$ mag). The mean extinction is used since we cannot directly determine the line of sight extinction from the cloud for these sources.

Once the extinction values are assigned, we use these values combined with the Weingartner & Draine (2001) extinction law for $R_V = 5.5$ to correct the photometry for extinction. The choice of the $R_V = 5.5$ law rather than the $R_V = 3.1$ law is motivated by several studies showing that the former is more appropriate for the dense regions in which stars form (e.g., Chapman et al. 2009). While the original extinction corrections in E09 only used the absorption cross section, here we adopt the sum of the absorption and scattering cross sections in order to correct for the total line of sight extinction.

Tables 1–3 list the absorption and scattering corrected spectral indices and photometry for each YSO. The 369 YSOs identified in this work were reclassified according to their newly corrected spectral index. We find 70 Class 0+I, 32 Flat, 231 Class II, and 36 Class III sources in Perseus. Although the number of sources in each class differs from E09, the fractions of each class compared to the total number of YSOs is not significantly different from those reported by E09 in comparing the five c2d clouds.

Perseus has a larger fraction, 19%, of Class 0+I sources compared to the other c2d star-forming clouds. Hsieh & Lai (2013) classified their 469 YSOs in Perseus using the same class definitions, reporting 99 Class 0+I, 49 Flat, 272 Class II, and 49 Class III sources (their Table 8). They find more YSOs in each category compared to the c2d list, however, the fractions of each class remain very similar to this work. Namely, Hsieh & Lai (2013) also find a large fraction, 21%, of Class 0+I sources. Table 4 gives the fraction of the total number of YSOs for each classification.

These observational YSO classifications are suggestive of physical stages of star formation. Heiderman & Evans (2015) used HCO^+ observations to classify Class 0+I and Flat sources identified in the c2d and Gould Belt (Dunham et al. 2015) *Spitzer* surveys of molecular clouds as physically embedded Stage 0+I (Robitaille et al. 2006) objects that retain envelope material. They find 72% of the *Spitzer* Class I and 48% of Flat sources are also Stage 0+I protostars.

YSO classification has also been connected to the physical nature of disks around young stars. Lada et al. (2006) and Teixeira et al. (2012) used α derived from IRAC data to place YSOs with optically thick disks and anemic disks into distinct categories. The thick and thin disk classifications developed by Lada et al. (2006) are very similar to the Class II and Class III definitions of Greene et al. (1994). Using these definitions, we find 228 YSOs with thick disks ($-0.5 > \alpha_{\text{IRAC}} \geq -1.8$) and 29 with anemic disks ($-1.8 > \alpha_{\text{IRAC}} \geq -2.56$) in Perseus. The IC 348 cluster region contains nearly half of these sources (126) and the majority of the thick disks (59%) in the cloud.

5. YSO DISTRIBUTION

5.1. Across the Cloud

More YSOs were identified in Perseus than in any of the other clouds studied in the c2d survey. However, it also covers the most area. Perseus, as previously reported in E09, has a density of 5.0 YSOs per square parsec, placing it behind Serpens and Ophiuchus in terms of number of YSOs per area. Table 4 lists the number of YSOs per square parsec, assuming a

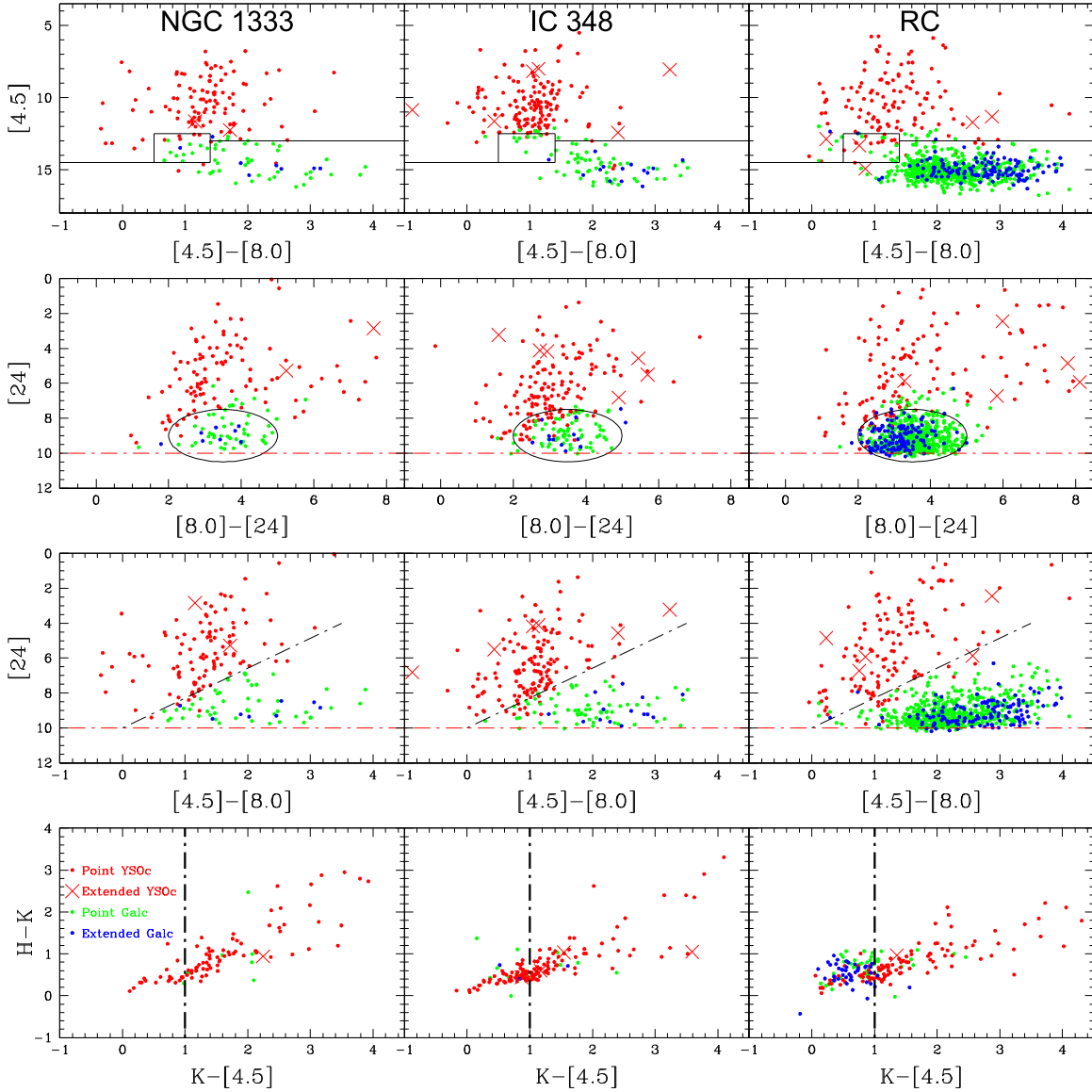


Figure 4. Color-color and color-magnitude diagrams for the IC 348, NGC 1333, and the RC regions used to identify extragalactic sources and thus identify YSOs in Perseus. H- and K-band data are from 2MASS. Lines and ellipses are cutoffs that differentiate galaxies and YSOs. Sources below the lines and inside the ellipses are assigned a higher probability of being extragalactic. Red points and crosses indicate sources that were identified as point and extended YSOs. Green and blue indicate point-like and extended extragalactic sources respectively.

distance of 250 pc, for each region of Perseus. If we adopt the distance found by Hirota et al. (2008) of 235 pc for NGC 1333, the density increases to 5.7 YSOs pc^{-2} .

As noted in Section 3, the YSOs in Perseus are not evenly distributed across the cloud (Figure 6). Instead there are two main sections with star formation activity. To the east lie B5, IC 348, and L1468. NGC 1333, B1, L1448, and L1455 are on the opposite end of the mapped region (Figure 7). The two clusters, IC 348 and NGC 1333, contain 67% of the YSOs in Perseus. NGC 1333 has the highest density of YSOs, 32 pc^{-2} . Many of the 122 YSOs in the RC are associated with the other known star-forming associations such as B1 (22), L1448 (5), and L1455 (11). L1455 has the lowest density of all the regions at 1.4 YSOs pc^{-2} .

Only two YSOs are found in the middle of Perseus far from the clusters and known star-forming associations (see Figure 7): index numbers 304 and 305 in Table 3 and E09. YSO 304 is within a few arcminutes of the dark cloud L1468. However,

there is no evidence in the literature of star formation activity in L1468. Both YSOs are found toward regions where the visual extinction is greater than 4 magnitudes and both are Class II sources. Hsieh & Lai (2013) identified three additional YSO candidates (their numbers 227, 228, and 231) in the mid-cloud region. One of their candidates (231) is within 2 arcmin of our YSO number 305. Section 6 discusses the mid-cloud region in terms of visual extinction and star formation.

5.2. By Class

Hsieh & Lai (2013) divided Perseus into eastern and western regions and concluded that western Perseus (including NGC 1333) has the greatest fraction of embedded sources (Class 0+I) of any of the c2d molecular clouds. The *Herschel Space Observatory* observed more infrared emission in its shorter wavelength bands (70 and $160 \mu\text{m}$) in eastern Perseus (IC 348) than the western end of the cloud indicating that the

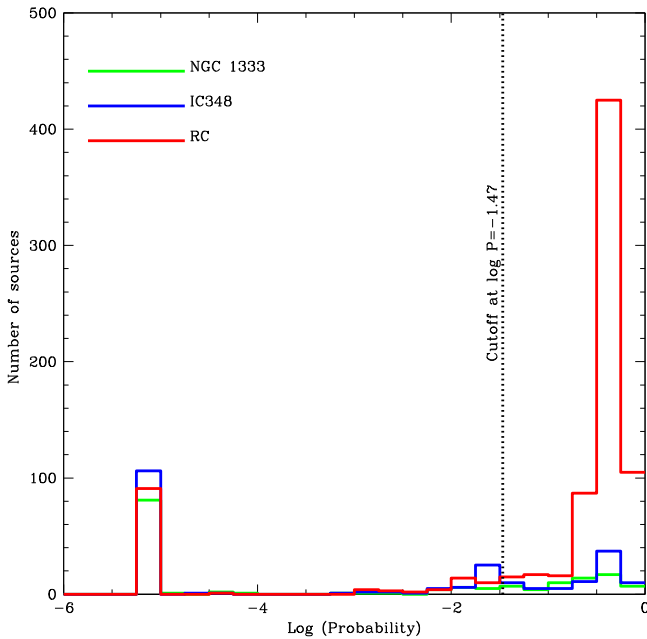


Figure 5. Plot of the number of sources vs. the unnormalized total “probability” of being an extragalactic source for Perseus. This proxy for probability is formed from the product of the individual probabilities from the color–magnitude diagrams in Figure 4 and other factors as described in Section 3. The green, blue, and red lines are the probability distributions toward NGC 1333, IC 348, and the RC respectively. The vertical dashed line is the cutoff to separate YSOs and extragalactic sources at $P = -1.47$.

eastern end is warmer (Di Francesco 2013). Further analysis of the *Herschel* data showed regions in the western end of the cloud (NGC 1333 and L1448) have the greatest fractions of Class 0+I YSOs (Sadavoy et al. 2013).

Figure 7 shows the locations of YSOs according to their classifications overlaid on the $8\,\mu\text{m}$ IRAC map. Named star-forming associations are labeled and the clusters and larger associations (B1 and L1455) used for analysis of the YSO populations in this work are outlined in the figure. Table 4 lists the regional number and fraction of YSOs for each class in the clusters, RC, B1, L1455, and the eastern and western sections of the clouds as well as the ratio of Class II to Class 0+I YSOs for the region. The charts in Figure 8 are a visual representation of the distribution of YSOs by class for regions listed in Table 4.

Our results agree with those of Hsieh & Lai (2013) and the *Herschel* studies (Di Francesco 2013; Sadavoy et al. 2013). By dividing the Perseus cloud into eastern and western sections along a line of R.A. at $3^{\text{h}}38^{\text{m}}00^{\text{s}}$ (Figure 7), we find three-quarters of the Class 0+I and Flat YSOs in the western section. The eastern section, an area of approximately 1.6 square degrees, includes IC 348 and contains the majority of the more evolved sources, 61% of Class II and 81% of Class III.

Assuming a constant birthrate of stars, the ratio of the number of Class II to Class 0+I YSOs is used as a relative age estimate between star-forming regions (Gutermuth et al. 2009). Class II sources are more abundant than Class 0+I YSOs in eastern Perseus by a ratio of 9.3 to 1. When we analyze the YSO population in the clusters, the Class II/(0+I) ratio is 9.5 in IC 348 but only 2.1 in NGC 1333, implying IC 348 is older. Gutermuth et al. (2009) found ratios of 9.0 and 2.7 for IC 348 and NGC 1333 respectively and both the separate IRAC (Jørgensen et al. 2006) and MIPS (Rebull et al. 2007) studies of Perseus agree that IC 348 contains a larger ratio of Class II to Class I sources. The Class II/(0+I) ratios are consistent with previous age estimates for the clusters (NGC 1333 < 1 Myr, Wilking et al. 2004 and IC 348 approx. 2 Myr, Lada et al. 2006).

We find more than twice the number of Class 0+I and Flat sources are associated with NGC 1333 as are associated with IC 348, as first suggested by the analysis of IRAC data alone (Jørgensen et al. 2006). Jørgensen et al. (2006) found that the majority of these more embedded sources were in the smaller star-forming regions in the RC, suggesting that these associations are the sites of the most recent star formation activity in the cloud. However, when Rebull et al. (2007) analyzed the MIPS data, they showed that the abundance of bright Class I and Flat sources is not higher in the RC, suggesting that the Jørgensen et al. (2006) result applies only to faint YSOs.

With the combined IRAC and MIPS data, as well as the extinction corrected source classifications, we find 40 Class 0+I and Flat sources in the defined NGC 1333 region and 46 in the RC. Further, we find the RC has a greater number of Class 0+I and Flat YSOs (28) with MIPS $24\,\mu\text{m}$ fluxes greater than 100 mJy compared to NGC 1333 (15). The Class II/(0+I) ratio in NGC 1333 (2.1) is nearly equal to that of the RC (2.2). Based solely on source counts in these regions, there is not an obvious implied age difference between NGC 1333 and the RC.

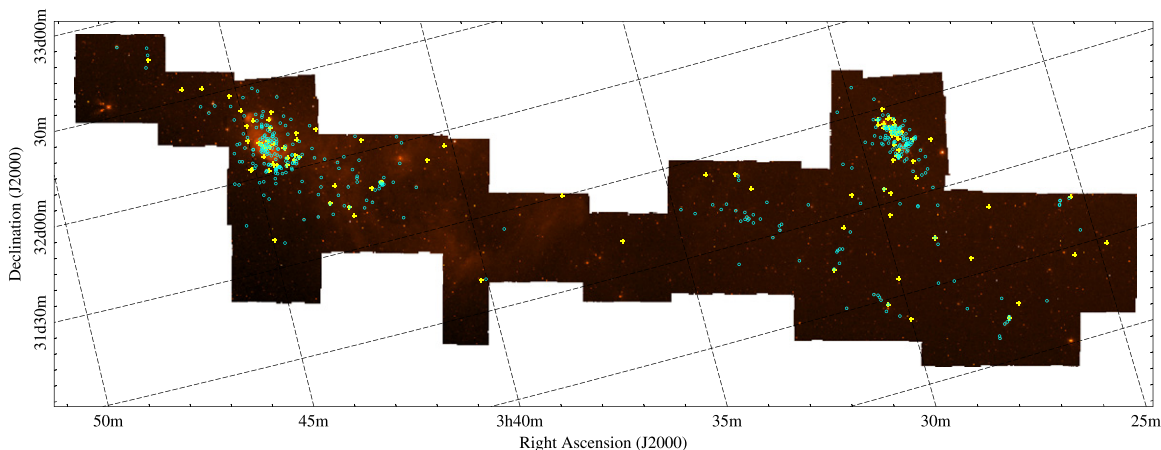


Figure 6. The 369 YSOs identified in this work (cyan circles) and the new candidate YSOs from Hsieh & Lai (2013) (yellow crosses) on the IRAC $4.5\,\mu\text{m}$ map of Perseus.

Table 3
YSOs in the RC

E09 Index	Source Name (SSTc2d +)	α	Class	IRAC ^a 3.6 μm	IRAC 4.5 μm	IRAC 5.8 μm	IRAC 8.0 μm	MIPS ^a 24 μm	MIPS 70 μm
121	J032519.52+303424.2	-0.14	Flat	3.6 \pm 0.26	4.4 \pm 0.27	5.3 \pm 0.31	7.0 \pm 0.38	13 \pm 1.4	...
122	J032522.32+304513.9	2.21	O+I	0.47 \pm 0.06	4.4 \pm 0.39	6.6 \pm 0.46	14 \pm 0.75	550 \pm 59	13000 \pm 1400
123	J032536.22+304515.7	1.51	O+I	0.69 \pm 0.26	3.8 \pm 0.5	5.1 \pm 0.5	6.6 \pm 0.67	220 \pm 33	...
124	J032536.49+304522.2	2.56	O+I	1.0 \pm 0.22	15 \pm 0.99	57 \pm 2.8	180 \pm 9.3	4500 \pm 480	25000 \pm 2600
125	J032538.83+304406.2	2.05	O+I	4.3 \pm 0.39	16 \pm 1.6	20 \pm 1.5	26 \pm 2.1	2100 \pm 220	32000 \pm 3400
126	J032539.12+304358.2	2.00	O+I	3.4 \pm 0.27	31 \pm 1.9	94 \pm 4.7	170 \pm 8.7	1400 \pm 160	...
127	J032637.47+301528.1	1.03	O+I	5.2 \pm 0.42	13 \pm 0.87	14 \pm 0.98	16 \pm 1.1	460 \pm 48	4400 \pm 600
128	J032738.25+301358.6	-0.40	II	90 \pm 6.3	97 \pm 6.9	100 \pm 7.0	120 \pm 8.7	390 \pm 41	1100 \pm 160
130	J032739.08+301303.1	2.46	O+I	0.83 \pm 0.07	12 \pm 0.93	25 \pm 1.4	32 \pm 1.6	2000 \pm 210	21000 \pm 2400
131	J032741.47+302016.8	-1.06	II	66 \pm 4.6	55 \pm 4.2	49 \pm 3.8	59 \pm 4.1	120 \pm 12	160 \pm 19
132	J032743.23+301228.9	2.23	O+I	1.1 \pm 0.10	7.3 \pm 0.50	15 \pm 0.83	37 \pm 1.7	880 \pm 92	7600 \pm 800
133	J032747.67+301204.5	-0.25	Flat	590 \pm 46	690 \pm 50	1000 \pm 56	1700 \pm 89	2000 \pm 210	1800 \pm 200
134	J032800.09+300847.0	-1.13	II	54 \pm 3.8	46 \pm 3.4	35 \pm 3.0	33 \pm 3.0	92 \pm 9.7	160 \pm 20
135	J032800.39+300801.3	0.98	O+I	19 \pm 1.3	36 \pm 2.0	57 \pm 2.8	92 \pm 4.5	430 \pm 45	700 \pm 76
137	J032834.49+310051.1	0.88	O+I	79 \pm 5.5	160 \pm 10	280 \pm 14	320 \pm 17	1400 \pm 140	2800 \pm 300
139	J032834.94+305454.5	-0.06	Flat	2.7 \pm 0.19	3.5 \pm 0.22	4.7 \pm 0.25	6.3 \pm 0.33	14 \pm 1.4	...
140	J032835.03+302009.9	-0.20	Flat	2.2 \pm 0.14	1.6 \pm 0.13	1.3 \pm 0.12	1.8 \pm 0.14	48 \pm 5.1	140 \pm 18
146	J032842.41+302953.2	-1.05	II	33 \pm 2.3	30 \pm 2.3	29 \pm 2.1	36 \pm 2.4	43 \pm 4.5	...
150	J032845.30+310541.9	1.09	O+I	1.7 \pm 0.13	3.6 \pm 0.26	3.4 \pm 0.24	3.6 \pm 0.25	240 \pm 26	1500 \pm 210
155	J032850.62+304244.7	-0.36	II	13 \pm 0.9	13 \pm 0.89	12 \pm 0.8	16 \pm 0.95	71 \pm 7.5	76 \pm 1.0
161	J032852.17+304505.5	-0.78	II	300 \pm 22	350 \pm 30	410 \pm 23	520 \pm 30	340 \pm 36	...
193	J032903.87+305629.8	-0.44	II	1.4 \pm 0.10	1.3 \pm 0.09	1.1 \pm 0.09	1.3 \pm 0.09	13 \pm 1.4	...
196	J032904.12+305612.8	-0.97	II	4.2 \pm 0.28	3.6 \pm 0.27	3.2 \pm 0.26	3.9 \pm 0.28	9.2 \pm 1.0	...
203	J032906.05+303039.2	0.64	O+I	0.89 \pm 0.06	1.3 \pm 0.08	2.3 \pm 0.14	5.3 \pm 0.26	24 \pm 2.5	110 \pm 19
244	J032923.48+313329.5	1.53	O+I	1.1 \pm 0.11	3.1 \pm 0.23	3.2 \pm 0.31	4.0 \pm 0.28	220 \pm 23	1200 \pm 160
248	J032928.88+305841.9	-1.05	II	5.0 \pm 0.35	4.6 \pm 0.33	4.7 \pm 0.33	7.5 \pm 0.43	14 \pm 1.5	...
256	J032946.00+310439.0	-0.89	II	33 \pm 2.3	29 \pm 2.1	25 \pm 2.0	25 \pm 2.0	42 \pm 4.4	96 \pm 14
257	J032951.82+313906.0	3.40	O+I	...	0.03 \pm 0.01	0.13 \pm 0.04	0.49 \pm 0.05	56 \pm 6.0	2000 \pm 290
259	J033015.14+302349.4	1.58	O+I	10 \pm 0.76	26 \pm 1.3	28 \pm 1.4	59 \pm 2.9	2100 \pm 220	5700 \pm 610
260	J033022.45+313240.5	0.28	Flat	1.7 \pm 0.12	2.2 \pm 0.13	2.8 \pm 0.17	5.7 \pm 0.28	21 \pm 2.2	...
261	J033024.08+311404.4	-1.20	II	5.3 \pm 0.37	4.2 \pm 0.35	3.9 \pm 0.32	5.2 \pm 0.36	5.5 \pm 0.61	...
262	J033025.97+310217.9	-2.44	III	75 \pm 5.3	48 \pm 4.4	32 \pm 3.9	20 \pm 3.8	4.8 \pm 0.53	...
263	J033027.14+302829.8	-0.16	Flat	22 \pm 1.4	20 \pm 1.3	14 \pm 1.1	12 \pm 1.1	500 \pm 52	950 \pm 100
264	J033032.68+302626.6	2.66	O+I	0.09 \pm	0.27 \pm 0	0.24 \pm 0.05	0.21 \pm 0.04	36 \pm 3.7	320 \pm 44
265	J033035.47+311558.6	-0.60	II	2.0 \pm 0.14	1.6 \pm 0.12	1.5 \pm 0.13	2.0 \pm 0.14	20 \pm 2.1	130 \pm 20
266	J033035.92+303024.4	-1.21	II	720 \pm 56	560 \pm 47	520 \pm 42	550 \pm 44	600 \pm 64	180 \pm 20
267	J033036.97+303127.7	-0.97	II	260 \pm 18	280 \pm 18	310 \pm 18	430 \pm 24	410 \pm 42	120 \pm 16
268	J033038.20+303211.9	-0.02	Flat	1.6 \pm 0.11	1.3 \pm 0.10	1.1 \pm 0.10	0.92 \pm 0.09	64 \pm 6.8	250 \pm 30
269	J033043.98+303247.0	-0.89	II	410 \pm 33	390 \pm 28	380 \pm 28	430 \pm 28	780 \pm 83	810 \pm 86
270	J033052.51+305417.8	-0.86	II	49 \pm 3.5	47 \pm 3.2	44 \pm 3.0	71 \pm 4.0	120 \pm 13	160 \pm 21
271	J033110.68+304940.6	-0.92	II	31 \pm 2.2	29 \pm 2.1	30 \pm 2.1	39 \pm 2.5	64 \pm 6.8	82 \pm 13
272	J033114.70+304955.4	-0.07	Flat	55 \pm 3.9	67 \pm 4.2	81 \pm 4.6	110 \pm 5.5	260 \pm 28	230 \pm 26
273	J033118.30+304939.5	-1.01	II	230 \pm 17	210 \pm 16	200 \pm 15	280 \pm 18	340 \pm 35	200 \pm 25
274	J033120.11+304917.7	-0.89	II	9.8 \pm 0.68	8.8 \pm 0.64	8.3 \pm 0.61	9.9 \pm 0.66	16 \pm 1.7	...
275	J033120.98+304530.1	1.48	O+I	0.19 \pm	1.1 \pm 0.09	1.1 \pm 0.09	0.82 \pm 0.08	17 \pm 1.7	4000 \pm 540
276	J033128.87+303053.3	-1.36	II	220 \pm 16	190 \pm 14	160 \pm 13	140 \pm 13	140 \pm 15	210 \pm 26
277	J033131.17+304411.1	-1.46	II	1.6 \pm 0.22	5.3 \pm 0.48	2.3 \pm 0.23	2.4 \pm 0.24	1.9 \pm 0.30	...
278	J033142.40+310624.9	-1.48	II	45 \pm 3.2	35 \pm 2.7	26 \pm 2.3	24 \pm 2.4	29 \pm 3.1	...
279	J033217.96+304947.5	0.86	O+I	0.56 \pm 0.11	0.56 \pm 0.19	...	1.7 \pm 0.14	15 \pm 1.6	1700 \pm 180
280	J033229.17+310240.8	0.16	Flat	16 \pm 1.2	23 \pm 1.8	29 \pm 2.0	43 \pm 3.0	210 \pm 22	1100 \pm 160
281	J033232.99+310221.7	-1.12	II	83 \pm 6.0	79 \pm 5.7	66 \pm 4.8	78 \pm 5.4	90 \pm 9.5	...
282	J033234.05+310055.8	-1.02	II	140 \pm 9.7	120 \pm 9.0	100 \pm 7.7	120 \pm 8.8	340 \pm 36	300 \pm 36
284	J033241.70+311046.3	-0.78	II	37 \pm 2.7	33 \pm 2.3	29 \pm 2.2	55 \pm 3.8	130 \pm 14	97 \pm 13
285	J033247.20+305916.3	-1.27	II	530 \pm 35	480 \pm 34	440 \pm 28	500 \pm 31	360 \pm 39	210 \pm 28
286	J033257.84+310608.3	0.33	O+I	1.2 \pm 0.08	1.3 \pm 0.08	1.4 \pm 0.10	1.6 \pm 0.1	17 \pm 1.7	83 \pm 14
287	J033306.41+310804.6	0.17	Flat	10 \pm 0.73	13 \pm 0.79	14 \pm 0.83	28 \pm 1.3	110 \pm 11	45 \pm 9.9
288	J033309.56+310531.2	0.70	O+I	0.76 \pm 0.05	0.67 \pm 0.05	0.71 \pm 0.07	2.0 \pm 0.12	89 \pm 9.3	100 \pm 14
289	J033312.84+312124.2	0.16	Flat	430 \pm 32	590 \pm 42	810 \pm 45	1400 \pm 78	4600 \pm 500	3400 \pm 370
290	J033313.80+312005.3	1.31	O+I	0.86 \pm 0.06	1.8 \pm 0.10	3.2 \pm 0.17	7.1 \pm 0.37	68 \pm 7.1	57 \pm 18
291	J033314.38+310710.9	2.72	O+I	0.23 \pm 0	1.3 \pm 0.09	2.5 \pm 0.19	5.5 \pm 0.39	130 \pm 14	830 \pm 120
292	J033316.44+310652.5	1.56	O+I	...	0.35 \pm 0.05	0.56 \pm 0.06	...	23 \pm 2.4	1800 \pm 270
293	J033316.65+310755.2	1.69	O+I	23 \pm 1.7	66 \pm 3.5	110 \pm 5.2	160 \pm 7.2	2000 \pm 210	6600 \pm 710
294	J033317.85+310931.9	2.90	O+I	0.24 \pm 0.02	8.6 \pm 0.44	46 \pm 2.3	130 \pm 6.7	770 \pm 82	12000 \pm 1300

Table 3
(Continued)

E09 Index	Source Name (SSTc2d +)	α	Class	IRAC ^a 3.6 μm	IRAC 4.5 μm	IRAC 5.8 μm	IRAC 8.0 μm	MIPS ^a 24 μm	MIPS 70 μm
295	J033320.32+310721.5	0.61	0+I	6.0 \pm 0.42	23 \pm 1.1	33 \pm 1.5	42 \pm 2.1	200 \pm 21	360 \pm 45
296	J033327.29+310710.2	1.82	0+I	3.4 \pm 0.24	9.0 \pm 0.46	10 \pm 0.51	16 \pm 0.79	1800 \pm 200	5500 \pm 590
297	J033330.41+311050.6	-1.04	II	1300 \pm 91	1300 \pm 92	1200 \pm 80	1200 \pm 81	980 \pm 100	520 \pm 59
298	J033341.29+311341.0	-0.93	II	100 \pm 7.2	100 \pm 6.7	90 \pm 5.8	95 \pm 6.2	170 \pm 19	180 \pm 25
299	J033346.92+305350.1	-1.17	II	4.9 \pm 0.34	4.1 \pm 0.31	3.7 \pm 0.31	3.9 \pm 0.31	6.2 \pm 0.67	...
300	J033351.07+311227.8	-2.16	III	42 \pm 3.0	29 \pm 2.4	19 \pm 2.1	13 \pm 2.1	5.5 \pm 0.60	...
301	J033401.66+311439.8	-1.16	II	100 \pm 7.1	95 \pm 6.8	100 \pm 6.7	120 \pm 7.5	110 \pm 11	91 \pm 16
302	J033430.78+311324.4	-1.25	II	15 \pm 1.1	13 \pm 0.96	13 \pm 0.93	15 \pm 1.0	13 \pm 1.4	...
303	J033449.84+311550.3	-1.48	II	76 \pm 5.8	51 \pm 4.7	37 \pm 4.1	37 \pm 4.2	52 \pm 5.4	40 \pm 11
304	J033915.81+312430.7	-1.07	II	22 \pm 1.5	19 \pm 1.3	14 \pm 1.1	19 \pm 1.3	34 \pm 3.6	...
305	J034001.49+311017.3	-1.54	II	15 \pm 1.1	12 \pm 0.9	9.0 \pm 0.79	8.4 \pm 0.8	7.5 \pm 0.82	...
306	J034109.13+314437.9	-0.89	II	670 \pm 49	570 \pm 48	540 \pm 39	520 \pm 39	930 \pm 98	2200 \pm 230
307	J034114.11+315946.3	-2.09	III	50 \pm 3.5	32 \pm 3.0	23 \pm 2.7	19 \pm 2.7	9.6 \pm 1.0	...
308	J034119.19+320203.8	-1.45	II	23 \pm 1.7	21 \pm 1.5	17 \pm 1.3	16 \pm 1.3	10 \pm 1.1	...
309	J034124.42+315327.9	-1.06	II	4.0 \pm 0.28	3.9 \pm 0.26	3.5 \pm 0.25	3.7 \pm 0.27	3.0 \pm 0.42	...
310	J034139.17+313610.7	-1.15	II	51 \pm 3.5	36 \pm 3.1	30 \pm 2.9	53 \pm 3.6	150 \pm 16	...
311	J034141.09+314804.6	-0.16	Flat	4.7 \pm 0.33	6.6 \pm 0.39	8.0 \pm 0.45	11 \pm 0.55	13 \pm 1.4	...
312	J034153.26+315019.2	-0.38	II	4.0 \pm 0.29	4.3 \pm 0.28	4.7 \pm 0.29	6.8 \pm 0.38	12 \pm 1.3	...
313	J034155.71+314811.4	0.28	Flat	24 \pm 1.7	32 \pm 1.9	42 \pm 2.3	62 \pm 3.2	140 \pm 15	250 \pm 43
314	J034157.44+314836.7	-1.20	II	580 \pm 48	530 \pm 39	480 \pm 34	480 \pm 34	330 \pm 34	180 \pm 29
315	J034157.75+314800.8	-1.11	II	92 \pm 6.7	85 \pm 5.9	77 \pm 5.3	98 \pm 6.2	140 \pm 15	...
316	J034158.67+314821.4	0.47	0+I	2.9 \pm 0.2	4.4 \pm 0.26	6.2 \pm 0.34	10 \pm 0.5	43 \pm 4.4	...
317	J034201.01+314913.4	-1.42	II	7.8 \pm 0.55	6.4 \pm 0.48	5.4 \pm 0.45	5.4 \pm 0.45	5.3 \pm 0.61	...
318	J034202.17+314802.1	1.23	0+I	1.3 \pm 0.09	1.6 \pm 0.10	2.9 \pm 0.17	9.1 \pm 0.45	140 \pm 14	240 \pm 36
319	J034204.34+314711.6	-1.02	II	19 \pm 1.4	18 \pm 1.3	17 \pm 1.2	22 \pm 1.4	25 \pm 2.6	...
320	J034210.69+314705.6	-1.10	II	6.6 \pm 0.46	6.2 \pm 0.4	6.1 \pm 0.38	7.4 \pm 0.45	5.0 \pm 0.62	...
321	J034219.27+314327.0	-0.88	II	84 \pm 5.8	74 \pm 5.2	64 \pm 4.6	79 \pm 5.2	140 \pm 15	110 \pm 25
322	J034220.32+320531.0	-1.26	II	15 \pm 1.1	12 \pm 0.95	9.2 \pm 0.85	12 \pm 0.94	20 \pm 2.1	...
323	J034223.33+315742.7	-2.08	III	52 \pm 3.7	34 \pm 3.1	25 \pm 2.9	22 \pm 2.8	9.4 \pm 1.0	...
324	J034227.12+314432.9	-1.22	II	21 \pm 1.5	15 \pm 1.2	11 \pm 1.0	8.7 \pm 1.0	56 \pm 6.0	...
325	J034232.10+315249.5	-1.43	II	1.8 \pm 0.12	1.4 \pm 0.11	1.2 \pm 0.12	1.5 \pm 0.12	1.1 \pm 0.28	...
326	J034232.91+314220.6	-1.19	II	39 \pm 2.8	33 \pm 2.4	26 \pm 2.1	27 \pm 2.2	51 \pm 5.4	...
327	J034233.13+315214.7	-1.07	II	3.9 \pm 0.27	3.1 \pm 0.23	2.4 \pm 0.22	2.9 \pm 0.24	7.7 \pm 0.85	...
328	J034234.19+315101.0	-1.19	II	3.4 \pm 0.24	2.5 \pm 0.20	1.7 \pm 0.19	1.7 \pm 0.19	7.1 \pm 0.79	...
329	J034236.47+315517.6	-1.21	II	3.1 \pm 0.22	2.4 \pm 0.19	2.3 \pm 0.19	2.5 \pm 0.24	3.6 \pm 0.45	...
330	J034244.50+315958.7	-1.49	II	2.7 \pm 0.18	2.3 \pm 0.17	2.0 \pm 0.15	1.8 \pm 0.16	1.1 \pm 0.28	...
331	J034249.18+315011.2	-1.54	II	26 \pm 1.9	20 \pm 1.6	17 \pm 1.4	17 \pm 1.5	15 \pm 1.6	...
332	J034254.67+314345.3	-2.22	III	26 \pm 1.8	17 \pm 1.5	12 \pm 1.4	7.5 \pm 1.4	3.6 \pm 0.55	...
333	J034255.95+315842.0	-0.84	II	510 \pm 38	430 \pm 35	450 \pm 32	650 \pm 40	190 \pm 20	2400 \pm 270
334	J034256.05+315644.8	0.06	Flat	4.0 \pm 0.29	6.2 \pm 0.36	9.2 \pm 0.48	18 \pm 0.87	13 \pm 1.3	...
335	J034301.94+314435.6	-1.15	II	3.9 \pm 0.27	3.6 \pm 0.25	3.5 \pm 0.25	4.0 \pm 0.27	3.4 \pm 0.49	...
336	J034306.77+314820.5	-2.40	III	25 \pm 1.8	17 \pm 1.4	11 \pm 1.3	7.1 \pm 1.2	2.0 \pm 0.32	...
338	J034321.47+314246.3	-1.50	II	6.9 \pm 0.48	5.5 \pm 0.42	4.6 \pm 0.38	5.2 \pm 0.41	3.3 \pm 0.45	...
339	J034322.22+314613.6	-1.15	II	36 \pm 2.5	33 \pm 2.3	27 \pm 2.0	31 \pm 2.1	38 \pm 4.0	...
346	J034344.48+314309.3	-0.50	II	130 \pm 11	230 \pm 13	240 \pm 14	330 \pm 17	550 \pm 59	470 \pm 53
376	J034406.47+314325.1	-2.39	III	22 \pm 1.7	16 \pm 1.3	10 \pm 1.2	7.1 \pm 1.1	2.1 \pm 0.30	...
415	J034427.90+322718.9	-1.18	II	25 \pm 1.8	24 \pm 1.6	18 \pm 1.4	25 \pm 1.6	29 \pm 3.1	...
442	J034435.34+322837.2	-0.16	Flat	0.42 \pm 0.04	1.3 \pm 0.07	0.74 \pm 0.08	1.1 \pm 0.11	3.9 \pm 0.47	...
465	J034443.06+313733.7	-1.29	II	7.4 \pm 0.58	5.8 \pm 0.51	5.0 \pm 0.43	5.4 \pm 0.45	9.5 \pm 1.0	...
474	J034452.00+322625.4	-1.62	III	14 \pm 1.3	12 \pm 0.87	8.6 \pm 0.77	7.5 \pm 0.73	5.7 \pm 0.64	...
489	J034513.51+322434.8	-1.14	II	5.9 \pm 0.41	4.7 \pm 0.36	3.6 \pm 0.33	3.8 \pm 0.33	5.5 \pm 0.63	...
496	J034533.47+314555.3	-1.24	II	4.1 \pm 0.31	3.7 \pm 0.27	3.1 \pm 0.26	3.2 \pm 0.25	4.9 \pm 0.57	...
498	J034536.83+322557.0	-1.32	II	140 \pm 12	120 \pm 9.0	84 \pm 7.9	97 \pm 7.9	200 \pm 21	...
500	J034548.27+322412.0	-0.97	II	1300 \pm 110	1200 \pm 91	930 \pm 83	990 \pm 78	3000 \pm 320	5500 \pm 580
501	J034558.25+322647.5	-1.39	II	8.9 \pm 0.73	7.8 \pm 0.66	7.0 \pm 0.58	6.4 \pm 0.55	4.9 \pm 0.58	...
502	J034657.38+324917.4	-1.36	II	7.1 \pm 0.50	5.9 \pm 0.45	4.7 \pm 0.41	4.3 \pm 0.4	5.7 \pm 0.64	...
503	J034658.51+324658.9	-1.54	II	8.3 \pm 0.58	6.1 \pm 0.50	5.2 \pm 0.47	5.5 \pm 0.48	4.3 \pm 0.51	...
504	J034705.43+324308.5	0.51	0+I	89 \pm 6.3	110 \pm 7.1	130 \pm 7.4	170 \pm 9.7	690 \pm 73	930 \pm 100
505	J034741.58+325144.1	1.30	0+I	560 \pm 49	1100 \pm 65	1800 \pm 92	2200 \pm 130	3900 \pm 410	11000 \pm 1200

Note.^a *Spitzer* flux densities in mJy.

(This table is available in machine-readable and Virtual Observatory (VO) forms.)

Table 4
Properties of the Regions

Region	Area ^a (pc ²)	YSOs		Density ^c (pc ⁻²)	Class 0+I		Flat		Class II		Class III		Ratio II/(0+I)
		N _{YSO}	Frac. ^b		N	N/N _{YSO} ^d	N	N/N _{YSO} ^d	N	N/N _{YSO} ^d	N	N/N _{YSO} ^d	
All of Perseus	73.5	369	1.00	5.0	70	0.19	32	0.09	231	0.63	36	0.10	3.3
IC 348	6.85	143	0.39	21	11	0.08	5	0.03	104	0.73	23	0.16	9.5
NGC 1333	3.24	104	0.28	32	28	0.27	12	0.12	59	0.57	5	0.05	2.1
RC	63.4	122	0.33	1.9	31	0.25	15	0.12	68	0.56	8	0.07	2.2
B1	7.62	22	0.06	2.9	10	0.45	3	0.14	8	0.36	1	0.05	0.8
L1455	7.62	11	0.03	1.4	5	0.45	2	0.18	4	0.36	0	0.00	0.8
Eastern Perseus	31.0	193	0.52	6.2	15	0.08	9	0.05	140	0.73	29	0.15	9.3
Western Perseus	42.5	176	0.48	4.1	55	0.31	23	0.13	91	0.52	7	0.04	1.7

^a Assuming a distance of 250 pc.

^b Fraction of the total number of YSOs in Perseus that are in the region.

^c N_{YSO} per area.

^d Fraction of the total number of YSOs in the region that are of the above classification.

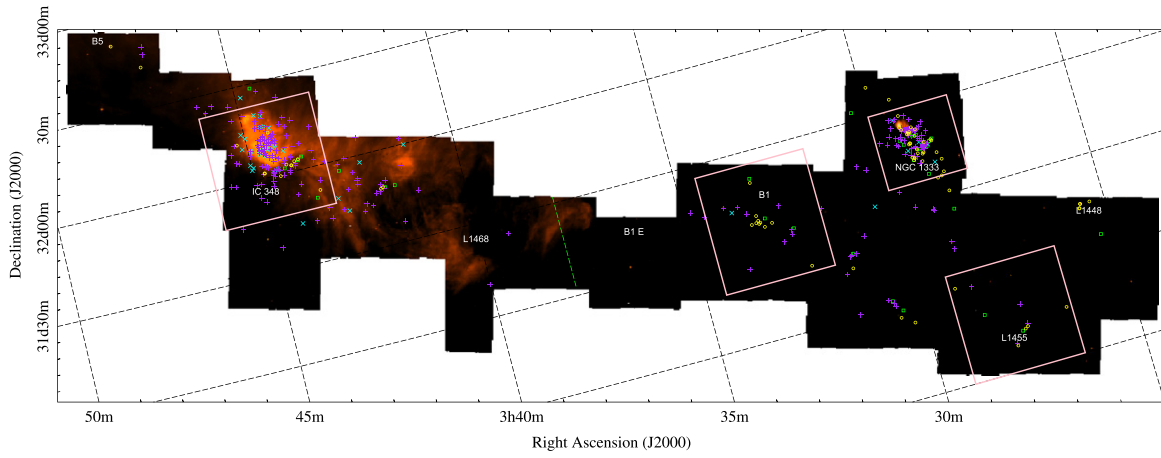


Figure 7. IRAC 8 μ m map of Perseus. Named regions are labeled. Pink boxes indicate the IC 348, NGC 1333, B1, and L1455 regions described in the text and listed in Table 4. The green dashed line denotes the R.A. used to divide the cloud into eastern and western regions in Section 5. The positions of the classified YSOs are indicated as follows: Class 0+I = yellow circle, Flat = green box, Class II = purple cross, Class III = cyan X.

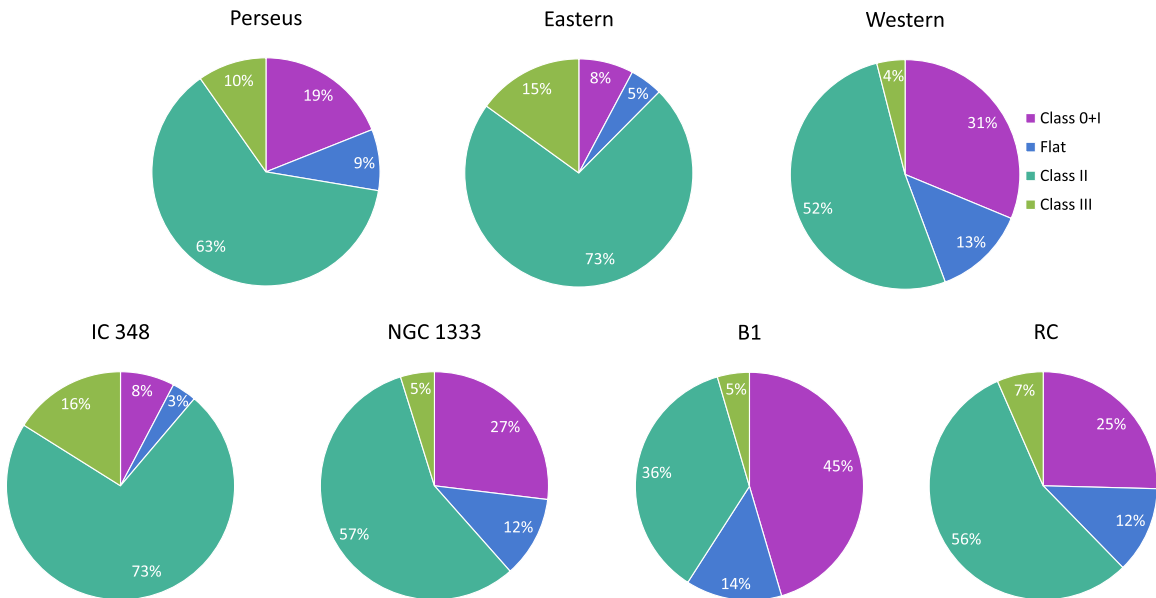


Figure 8. Fraction of YSOs in each region by classification. Colors indicate class: Class 0+I = purple, Flat = blue, Class II = teal, and Class III = green.

However, individual star-forming associations in the RC do contain higher fractions of Class 0+I sources than NGC 1333, suggesting a younger age for these regions and in agreement with Jørgensen et al. (2006). For example, L1448, at the far western edge of the *Spitzer* map, contains only embedded YSOs, 5 Class 0+I sources.

We defined large regions (0.4 square degrees, Figure 7) for the largest star-forming associations outside of the clusters, B1 and L1455. The B1 area is the same as the SCUBA 850 μm map of Sadavoy et al. (2013). Nearly half (45%) of the YSOs in the B1 and L1455 areas are Class 0+I sources in contrast with 27% in NGC 1333. The ratio of Class II to Class 0+I sources is only 0.8 in B1 and L1455. However, we caution that even with the broadly defined B1 and L1455 regions the total number of YSOs in these regions is relatively small (33).

We find Class III sources are most common in IC 348 in agreement with Jørgensen et al. (2006). Sixty four percent are found in the cluster. The RC contains only a few more Class III sources (8) than NGC 1333 (5). As noted previously, this is a lower limit for Class III sources in these regions since our data cannot identify young objects with star-like spectral energy distributions. Extensive X-ray observations or spectroscopic surveys of the Perseus cloud are needed to find the Class III sources missed by this survey.

Rebull (2015) cross-referenced a large number of NGC 1333 catalogs, including the *Spitzer* catalog, and classified YSOs with the combined data sets. Rebull identified more than twice as many YSOs (277) associated with the cluster than this work (104). The Rebull catalog encompasses a larger region than we define for NGC 1333, so some YSOs in Rebull (2015) are in our RC region. The YSOs in Rebull's catalog that we do not identify in this work were generally not detected in most or all of the *Spitzer* bands and were identified as YSOs with submillimeter, spectroscopic, or X-ray data. Rebull (2015) lists a large number of Class III sources in NGC 1333 that were identified as young by the Young Stellar Object Variability project (Rebull et al. 2014) with X-ray detections.

All of the NGC 1333 YSOs presented here are contained in the Rebull (2015) catalog and the classifications are generally consistent. Rebull (2015) classifies YSOs using the spectral index definitions from Greene et al. (1994) as in Section 4, however, α is defined from the observed SED without any reddening correction. Rebull places 15 YSOs in a different class than this work due to slightly greater values of α . For example, seven of our Class II sources are placed in the Flat category by Rebull (2015). The Rebull (2015) fractions of Class I and Flat sources in the cluster are consistent with this work. However, Rebull finds a much larger fraction of Class III sources in NGC 1333, 29%, because of the greater number of Class III sources identified with X-ray data.

6. EXTENDED EMISSION

Several studies have placed the large-scale nebulous emission in the IRAC 8 μm and MIPS 24 μm maps (Figures 1, 6, and 9) of Perseus in the context of star formation and related phenomena. The c2d team compared the IRAC and MIPS extended emission with areas of high extinction (Jørgensen et al. 2006; Rebull et al. 2007). They found no clear correlation at shorter wavelengths; however, the 160 μm mosaic revealed emission that matched extinction maps of the cloud (Rebull et al. 2007). More recently, the Coordinated Molecular Probe

Line Extinction and Thermal Emission (COMPLETE) team used the *Spitzer* maps of Perseus to help identify shells and bubbles in the cloud as part of their CO survey (Arce et al. 2011). They found that some of the arc-like nebulosities seen in the IRAC and MIPS maps are related to the edges of shells created by stellar winds.

Figure 9 shows A_v contours overlaid on the MIPS 24 μm map of Perseus. The contours are derived from an extinction map produced by the c2d team using 2MASS and *Spitzer* data. The visual extinctions toward sources classified as stars by c2d (see Figure 3) were convolved with a Gaussian beam to create extinction maps of the entire cloud (Evans et al. 2007). While there are bright regions of 24 μm emission at high extinction, many areas of high extinction ($A_v > 8$ mag), such as B1-E, show little to no extended emission.

Furthermore, the IRAC and MIPS extended emission is not necessarily correlated with star formation in Perseus. Most notably, the middle region of Perseus, between $3^{\text{h}}37^{\text{m}}00^{\text{s}}$ and $3^{\text{h}}41^{\text{m}}00^{\text{s}}$, contains only two Class II YSOs (see Section 5) despite bright extended emission at 8 and 24 μm (Figures 6 and 9).

CO and infrared maps show extended emission and some areas of high extinction in this middle region (e.g., Ridge et al. 2006a). The region also contains dark clouds such as L1468 and B1-E (Figure 7). However, there has been little evidence found of star formation, suggesting that the structure in the middle region is perhaps not filamentary enough to form stars (Di Francesco 2013). The COMPLETE survey highlights the lack of ^{13}CO in the mid-region of Perseus as corresponding to a shell, CPS 5, created by a nearby O or B star (Goodman et al. 2009; Arce et al. 2011). The size and location of CPS 5 is indicated on Figure 9 against the 24 μm image of Perseus.

Enoch et al. (2006) mapped Perseus at 1.1 mm and found no dense clumps in the middle of Perseus. Sadavoy et al. (2012) studied the B1-E association, located to the east of NGC 1333 and B1, toward the midsection of the cloud as shown in Figure 1, as part of the *Herschel Space Observatory* Gould Belt survey and found it to contain dense cores but no young stars. Figure 9 shows high extinction (mean $A_v \approx 10$ mag) toward B1-E, however, we do not find any YSOs in the region. Hsieh & Lai (2013), did report one YSO candidate in the region (their 227) using the c2d data.

It has been further postulated that Perseus may consist of two separate clouds that are not physically associated (e.g., Enoch et al. 2006; Kirk et al. 2006) or possibly a chain of clouds at a range of distances (250–350 pc) along the line of sight (Arce et al. 2011). If this is the case, the central region of Perseus as seen from Earth may be a physical gap between clouds. These scenarios would naturally explain the lack of YSOs in the mid-regions of Perseus. However, following the lead of earlier papers in this series and other recent surveys of Perseus mentioned here, we continue to assume the entire mapped region to be associated and at the same distance, while acknowledging the complexities of such a large cloud.

7. CLOUD STRUCTURE AND RELATION TO STAR FORMATION

7.1. Extinction Patterns

Histograms of visual extinction (A_v) toward IC 348, NGC 1333, the RC, and all of Perseus using stars observed with

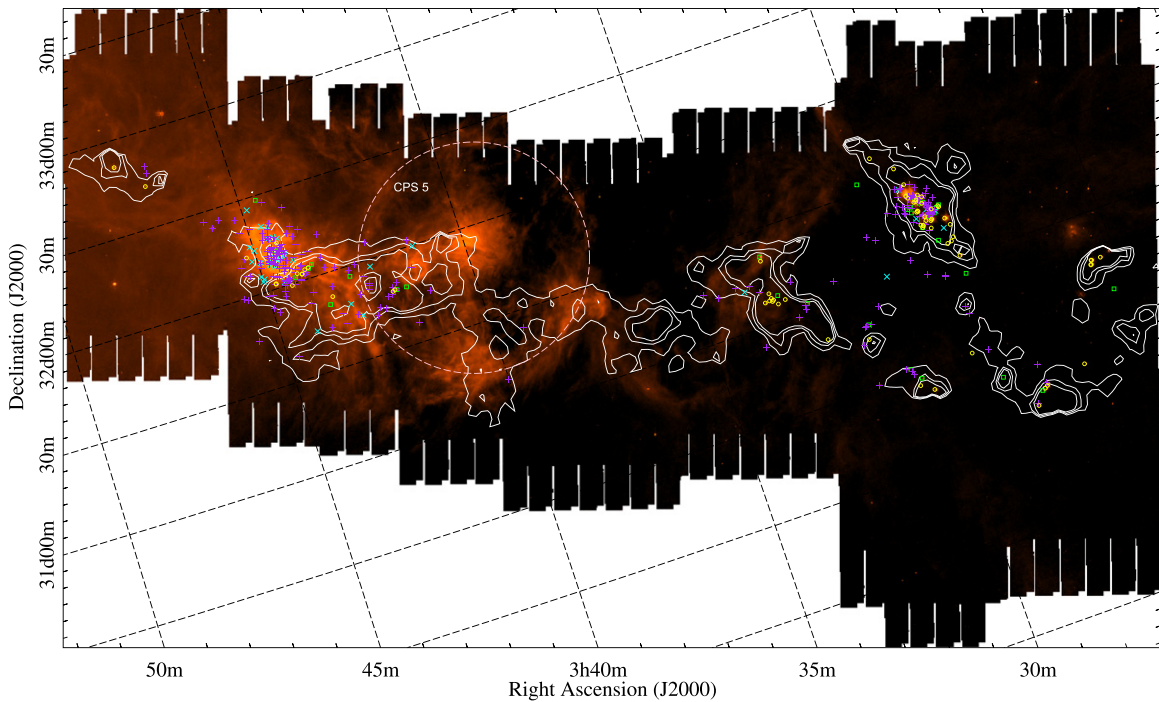


Figure 9. 24 μm map of Perseus overlaid with $A_v = 4, 6,$ and 8 mag contours derived from 2MASS and *Spitzer* data. The positions of the classified YSOs are indicated as follows: Class 0+I = yellow circle, Flat = green box, Class II = purple cross, Class III = cyan X. The size and location of the CO shell CPS 5 discussed in Section 6 is indicated by the large dashed circle.

IRAC and MIPS are presented in Figure 3. The A_v was measured along lines of sight through the cloud using the 2MASS and *Spitzer* spectral energy distribution of sources classified as stars and adopting the Weingartner & Draine (2001) extinction law, $R_v = 5.5$ mag (Evans et al. 2007). The histograms are presented as a fractional number of stars versus A_v . In this work, we limited our data collection by artificially setting the edge of the cloud at the $A_v = 2$ mag contour.

The histograms peak near $A_v = 5$ mag and have a tail to higher extinction. Many authors (Schnee et al. 2005; Ridge et al. 2006a, 2006b; Goodman et al. 2009; Kainulainen et al. 2009; Froebrich & Rowles 2010; Sadavoy et al. 2014) have presented extinction histograms for Perseus using 2MASS, IRAS, and *Herschel* infrared, as well as CO, data in comparison to log-normal probability distribution functions. Log-normal distributions at low column densities suggest the importance of turbulence in the cloud structure (e.g., Ostriker et al. 2001). Several of the studies (e.g., Kainulainen et al. 2009; Froebrich & Rowles 2010; Sadavoy et al. 2014) also show tails above log-normal distributions at higher A_v (≥ 5 mag), implying that perhaps self-gravity becomes more important as clouds begin to form stars (Klessen 2000; Federrath et al. 2008). Because of the $A_v = 2$ mag cutoff in our data, the histograms in Figure 3 represent mostly the higher A_v tail of the distribution.

We find mean A_v values of 10.3, 11.7, 15.5, and 10.1 mag for all of Perseus, IC 348, NGC 1333, and the RC respectively. The histogram of extinction for NGC 1333 (green in Figure 3) peaks at a higher A_v of 7.5 mag, has a larger mean A_v , and a larger tail to high extinction than the other regions. These features indicate different physical conditions in NGC 1333 and IC 348 (Goodman et al. 2009) and point to the recent star formation history of NGC 1333.

7.2. Threshold for Star Formation

Recent studies of molecular clouds, including Perseus, have suggested an extinction threshold for low-mass star formation (e.g., Kirk et al. 2006, Enoch et al. 2008, Heiderman et al. 2010, Lada et al. 2010, 2013, Evans et al. 2014; see also Section 8 of the recent review by Dunham et al. 2014). This threshold ranges from $A_v = 4$ –7 mag, below which very few or no dense cores are found. Kirk et al. (2006) found submillimeter clumps in Perseus only where $A_v \geq 5$ –7 mag and suggested a threshold of $A_v = 5$ mag linked to magnetic support of the clump, where there is only enough time for ambipolar diffusion if extinction is near the threshold extinction. Figure 9 shows our classified YSOs as well as $A_v = 4, 6,$ and 8 mag contours from the c2d extinction map (see Section 6) on the 24 μm mosaic of Perseus.

Using the background star extinctions averaged over $270''$ as in Heiderman & Evans (2015), we determined the A_v at the source position for each Class 0+I and Flat YSO, since these extinctions cannot be determined directly. Extinction values for Class II and III sources were previously collected from the literature in Evans et al. (2009). Fifty six percent of all the YSOs in Perseus are found toward an $A_v \geq 5$ mag.

The distribution of the Class 0+I and Flat YSOs, those sources that are least likely to have dispersed from their place of origin, as a function of A_v is shown in Figure 10. 91% of the Class 0+I and Flat sources are found toward $A_v \geq 5$ mag. Only three Class 0+I and six Flat YSOs are found at $A_v < 5$ mag. Heiderman & Evans (2015) report 75% of 535 Class 0+I and Flat sources in the c2d plus Gould Belt sample (Dunham et al. 2015), including the Perseus YSOs in this work, are found toward $A_v > 8$ mag. We find 85% of the Perseus Class 0+I and Flat sources are found toward $A_v > 8$ mag. These results agree with studies identifying dense cores only in regions of high extinction in Perseus (Hatchell et al. 2005; Kirk et al. 2006;

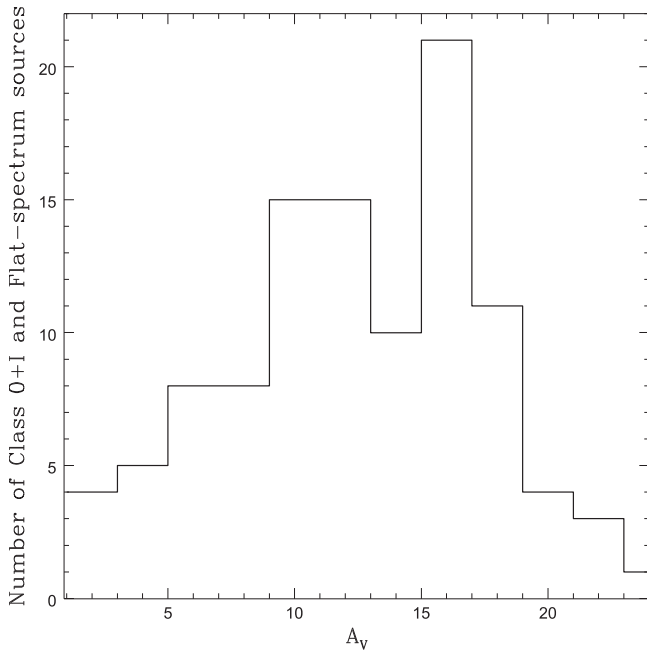


Figure 10. Distribution of Class 0+I and Flat YSOs as a function of visual extinction at the source position using the background star extinctions averaged over $270''$. 91% of these sources are found toward $A_v \geq 5$ mag.

Enoch et al. 2008; Heiderman et al. 2010) and support the idea of a threshold extinction near $A_v = 5$ –8 mag.

8. SUMMARY

We present IRAC and MIPS data from 3.6 to $70 \mu\text{m}$ of the Perseus molecular cloud and give a broad overview of the current star formation in the region. Perseus contains 369 YSOs and has a density of 5 YSOs per square parsec. Tables 1–3 list updated extinction corrected photometry for the YSOs including both absorption and scattering cross sections. While Perseus has a large fraction of embedded Class 0+I sources (19%), 63% of the objects in the cloud are classified as Class II YSOs.

Perseus contains a variety of star-forming environments. IC 348 and the eastern end of the cloud are shrouded in extended nebulosity at the longer *Spitzer* wavelengths. However, the IC 348 region contains fewer embedded sources and the majority of the Class II (73%) and III (64%) objects in Perseus, consistent with previous age estimates of 2 Myr (Lada et al. 2006). The NGC 1333 cluster, suggested to be <1 Myr (Wilking et al. 2004), contains more than twice the number of Class 0+I and Flat sources than IC 348. The ratios of Class II to Class 0+I YSOs (9.5 in IC 348 and 2.1 in NGC 1333) are also consistent with the relative age estimates of the clusters.

We find that 56% of all the YSOs and 91% of the Class 0+I and Flat spectrum sources in Perseus are in regions where the $A_v \geq 5$ mag, consistent with an extinction threshold for early stage star formation suggested by other authors (e.g., Enoch et al. 2008; Sadavoy et al. 2014; Heiderman & Evans 2015). However, the mid-cloud region is nearly devoid of star formation activity despite regions where the visual extinction ranges from $A_v = 5$ –20 mag.

Support for this work, part of the *Spitzer* Legacy Science Program, was provided by NASA through contracts 1224608, 1230782, and 1230779 issued by the Jet Propulsion Laboratory, California Institute of Technology, under NASA contract 1407. K.E.Y. and C.H.Y. acknowledge support from a Louisiana Space Consortium Research Enhancement Award through NASA EPSCoR grant number NNX10AI40H. M.M. D. acknowledges support from the Submillimeter Array through an SMA postdoctoral fellowship. N.J.E. acknowledges support from a grant from the National Science Foundation, AST-1109116. We would like to thank the anonymous referee for comments that improved the focus and clarity of this work.

Facility: *Spitzer*

REFERENCES

- Arce, H. G., Borkin, M. A., Goodman, A. A., Pineda, J. E., & Beaumont, C. N. 2011, *ApJ*, **742**, 105
- Chapman, N. L., Mundy, L. G., Lai, S.-P., & Evans, N. J., II 2009, *ApJ*, **690**, 496
- Chen, X., Arce, H. G., Zhang, Q., et al. 2010, *ApJ*, **715**, 1344
- Di Francesco, J. 2013, *Star Formation Newsl.* 252, <http://www.ifa.hawaii.edu/reipurth/newsletter.htm>
- Dunham, M. M., Allen, L. E., Evans, N. J., III, et al. 2015, *ApJS*, submitted
- Dunham, M. M., Arce, H. G., Allen, L. E., et al. 2013, *AJ*, **145**, 94
- Dunham, M. M., Crapsi, A., Evans, N. J., II, et al. 2008, *ApJS*, **179**, 249
- Dunham, M. M., Stutz, A. M., Allen, L. E., et al. 2014, in *Protostars and Planets VI*, ed. H. Beuther et al. (Tucson, AZ: Univ. Arizona Press)
- Enoch, M. L., Evans, N. J., II, Sargent, A. I., et al. 2008, *ApJ*, **684**, 1240
- Enoch, M. L., Evans, N. J., II, Sargent, A. I., & Glenn, J. 2009, *ApJ*, **692**, 973
- Enoch, M. L., Glenn, J., Evans, N. J., II, et al. 2007, *ApJ*, **666**, 982
- Enoch, M. L., Lee, J.-E., Harvey, P., Dunham, M. M., & Schnee, S. 2010, *ApJL*, **722**, L33
- Enoch, M. L., Young, K. E., Glenn, J., et al. 2006, *ApJ*, **638**, 293
- Evans, N. J., II, Allen, L. E., Blake, G. A., et al. 2003, *PASP*, **115**, 965
- Evans, N. J., II, Dunham, M. M., Jørgensen, J. K., et al. 2009, *ApJS*, **181**, 321
- Evans, N. J., II, Harvey, P. M., Dunham, M. M., et al. 2007, *Final Delivery of Data from the c2d Legacy Project: IRAC and MIPS*, (Pasadena, CA: SSC)
- Evans, N. J., II, Heiderman, A., & Vutisalchavakul, N. 2014, *ApJ*, **782**, 114
- Fazio, G. G., Hora, J. L., Allen, L. E., et al. 2004, *ApJS*, **154**, 10
- Federrath, C., Glover, S. C. O., Klessen, R. S., & Schmidt, W. 2008, *PhST*, **132**, 014025
- Froeberich, D., & Rowles, J. 2010, *MNRAS*, **406**, 1350
- Goodman, A. A., Pineda, J. E., & Schnee, S. L. 2009, *ApJ*, **692**, 91
- Greene, T. P., Wilking, B. A., Andre, P., Young, E. T., & Lada, C. J. 1994, *ApJ*, **434**, 614
- Gutermuth, R., Megeath, S. T., Myers, P. C., et al. 2009, *ApJS*, **184**, 18
- Gutermuth, R., Myers, P. C., Megeath, S. T., et al. 2008, *ApJ*, **674**, 336
- Harvey, P. M., Chapman, N., Lai, S.-P., et al. 2006, *ApJ*, **644**, 307
- Harvey, P. M., Merin, B., Huard, T. L., et al. 2007, *ApJ*, **663**, 1149
- Hatchell, J., Fuller, G. A., Richer, J. S., Harries, T. J., & Ladd, E. F. 2007, *A&A*, **468**, 1009
- Hatchell, J., Richer, J. S., Fuller, G. A., et al. 2005, *A&A*, **440**, 151
- Heiderman, A., & Evans, N. J., II, *ApJ*, **806**, 231
- Heiderman, A., Evans, N. J., II, Allen, L. E., Huard, T., & Heyer, M. 2010, *ApJ*, **723**, 1019
- Hirota, T., Bushimata, T., Choi, Y.-K., et al. 2008, *PASJ*, **60**, 37
- Hirota, T., Honma, M., Imai, H., et al. 2011, *PASJ*, **63**, 1
- Hsieh, T.-H., & Lai, S.-P. 2013, *ApJS*, **205**, 5
- Infrared Science Archive, 2007, *c2d Spitzer and Ancillary Data Catalog* (Pasadena, CA: IPAC), <http://irsa.ipac.caltech.edu/data/SPITZER/C2D/>
- Jørgensen, J. K., Harvey, P. M., Evans, N. J., II, et al. 2006, *ApJ*, **645**, 1246
- Jørgensen, J. K., Johnstone, D., Kirk, H., & Myers, P. C. 2007, *ApJ*, **656**, 293
- Kainulainen, J., Alves, J., Beuther, H., Henning, T., & Schuller, F. 2011, *A&A*, **536**, A48
- Kainulainen, J., Beuther, H., Henning, T., & Plume, R. 2009, *A&A*, **508**, L35
- Kirk, H., Johnstone, D., & Di Francesco, J. 2006, *ApJ*, **646**, 1009
- Klessen, R. S. 2000, *ApJ*, **535**, 869
- Lada, C. J., Lombardi, M., & Alves, J. F. 2010, *ApJ*, **724**, 687
- Lada, C. J., Lombardi, M., Roman-Zuniga, C., et al. 2013, *ApJ*, **778**, 133
- Lada, C. J., Muench, A. A., Luhman, K. L., et al. 2006, *AJ*, **131**, 1574
- Ladd, E. F., Lada, E. A., & Myers, P. C. 1993, *ApJ*, **410**, 168

- Lonsdale, C. J., Smith, H. E., Rowan-Robinson, M., et al. 2003, [PASP](#), **115**, 897
- Oliveira, I., Merín, B., Pontoppidan, K. M., et al. 2009, [ApJ](#), **691**, 672
- Oliveira, I., Pontoppidan, K. M., Merín, B., et al. 2010, [ApJ](#), **714**, 778
- Ostriker, E. C., Stone, J. M., & Gammie, C. F. 2001, [ApJ](#), **546**, 980
- Padoan, P., Bally, J., Billawala, Y., Juvela, M., & Nordlund, A. 1999, [ApJ](#), **525**, 318
- Pineda, J. E., Arce, H. G., Schnee, S., et al. 2011, [ApJ](#), **743**, 201
- Pineda, J. E., Caselli, P., & Goodman, A. A. 2008, [ApJ](#), **679**, 481
- Rebull, L. M. 2015, [AJ](#), **150**, 17
- Rebull, L. M., Cody, A. M., Covey, K. R., et al. 2014, [ApJ](#), **148**, 92
- Rebull, L. M., Stapelfeldt, K. R., Evans, N. J., II, et al. 2007, [ApJS](#), **171**, 447
- Robitaille, T. P., Whitney, B. A., Indebetouw, R., Wood, K., & Denzmore, P. 2006, [ApJS](#), **167**, 256
- Rieke, G., et al. 2004, [ApJS](#), **154**, 25
- Ridge, N. A., Di Francesco, J., Kirk, H., et al. 2006a, [AJ](#), **131**, 2921
- Ridge, N. A., Schnee, S. L., Goodman, A. A., & Foster, J. B. 2006b, [ApJ](#), **643**, 932
- Sadavoy, S., Di Francesco, J., Andre, P., & Pezzuto, S. 2013, in *Protostars and Planets VI*, ed. H. Beuther et al. (Tucson, AZ: Univ. Arizona Press), poster #IS031
- Sadavoy, S., Di Francesco, J., Andre, P., et al. 2012, [A&A](#), **540**, A10
- Sadavoy, S., Di Francesco, J., Andre, P., et al. 2014, [ApJL](#), **787**, L18
- Sargent, A. I. 1979, [ApJ](#), **233**, 163
- Schnee, S. L., Ridge, N. A., Goodman, A. A., & Li, J. G. 2005, [ApJ](#), **634**, 442
- Teixeira, P. S., Lada, C. J., Marengo, M., & Lada, E. A. 2012, [A&A](#), **540**, A83
- Weingartner, J. C., & Draine, B. T. 2001, [ApJ](#), **548**, 296
- Werner, M. W., Roellig, T. L., Low, F. J., et al. 2004, [ApJS](#), **154**, 1
- Willing, B. A., Meyer, M. R., Green, T. P., Mikhail, A., & Carlson, G. 2004, [AJ](#), **127**, 1131
- Young, K. E., Harvey, P. M., Brooke, T. Y., et al. 2005, [ApJ](#), **628**, 283